UNIVERSIDAD DE CHILE
FACULTAD DE CIENCIAS FÍSICAS Y MATEMÁTICAS
DEPARTAMENTO DE FÍSICA

TRANSPORT PROPERTIES OF WEYL SEMIMETALS

TESIS PARA OPTAR AL GRADO DE MAGÍSTER EN CIENCIAS, MENCIÓN FÍSICA

JOSÉ LUIS CHESTA LÓPEZ

PROFESOR GUÍA:
LUIS E. F. FOÀ TORRES

MIEMBROS DE LA COMISIÓN:
ÁLVARO S. NÚÑEZ VÁSQUEZ
FRANCISCO MUÑOZ SAEZ
PEDRO ORELLANA DINAMARCA

Este trabajo ha sido parcialmente financiado por Proyecto Fondecyt Regular 1150072, Proyecto Fondecyt Regular 1170917 y Proyecto Basal No. FB 0807-CEDENNA.

SANTIAGO DE CHILE
2019

RESUMEN DE LA TESIS PARA OPTAR
AL TÍTULO DE MAGÍSTER EN CIENCIAS, MENCIÓN FÍSICA
POR: JOSÉ LUIS CHESTA LÓPEZ
FECHA: 2019
PROF. GUÍA: SR. LUIS E. F. FOÀ TORRES

TRANSPORT PROPERTIES OF WEYL SEMIMETALS

Los semimetales de Weyl son una nueva fase topológica paradigmática de la materia que contiene un espectro sin brecha energética. Una de sus características más significativas es la presencia de arcos de Fermi, los cuales tienen asociados estados de superficie con propiedades topológicas exclusivas que los diferencian de otros tipos de materiales topológicos. Se espera que el control sobre estas propiedades electrónicas exóticas de un semimetal de Weyl ayude al desarrollo de dispositivos novedosos de información cuántica.

En la primera parte de esta tesis, introducimos el rol de la topología en el contexto de teoría de bandas topológicas. Revisamos como definir invariantes topológicos, cómo aparecen efectos Hall cuánticos, y estudiamos en mayor detalle dos de los mejores conocidos ejemplos de materiales topológicos: el aislante de Chern y el grafeno.

En la segunda parte de esta tesis estudiamos algunas de las propiedades más significativas de los semimetales de Weyl, mostrando cómo estos materiales necesitan romper ya sea simetría de inversión espacial o simetría de reversión temporal, y algunas de las consecuencias directas de la estructura electrónica como la aparición de un efecto Hall cuántico anómalo y la anomalía quiral. Además, revisamos los descubrimientos experimentales de los últimos años.

En la tercera parte de esta tesis, cambiamos el foco al transporte cuántico, más específicamente a una perspectiva de transporte coherente. Deducimos el origen de la fórmula de Landauer-Büttiker y dilucidamos por qué una respuesta multiterminal es necesaria para medir propiedades de transporte no locales en un material. La parte crucial de esta sección es que nos entrega las herramientas matemáticas para calcular respuestas al transporte en semimetales de Weyl.

El último capítulo consiste en la investigación original llevada a cabo en esta tesis. Aquí, reportamos sobre simulaciones atomísticas de la conductancia dc y la respuesta Hall de una versión simplificada de un semimetal de Weyl. Usando teoría de scattering, mostramos que emerge una conductancia de Hall cuantizada y una conductancia longitudinal no nula asociadas a los estados de superficie de arcos de Fermi con una robustez notable que persiste a altas concentraciones de defectos en el sistema. Adicionalmente, predecimos que en un bloque finito de semimetal de Weyl que quiebre simetría de reversión temporal, aparecen corrientes persistentes que están completamente determinadas por el tamaño del sistema y los parámetros de la red.

RESUMEN DE LA TESIS PARA OPTAR
AL TÍTULO DE MAGÍSTER EN CIENCIAS, MENCIÓN FÍSICA
POR: JOSÉ LUIS CHESTA LÓPEZ
FECHA: 2019
PROF. GUÍA: SR. LUIS E. F. FOÀ TORRES

TRANSPORT PROPERTIES OF WEYL SEMIMETALS

Weyl semimetals are a new paradigmatic topological phase of matter featuring a gapless spectrum. One of its most distinctive features is the presence of Fermi arc surface states with unique topological properties that differentiate them to other types of topological materials. Control over the exotic electronic properties of a Weyl semimetal is expected to lead to the development of novel quantum information devices.

In the first part of this thesis, we introduce the role of topology on the context of topological band theory. We review how to define topological invariants, how do integer quantum Hall effects arise, and study in more detail the two best-known examples of topological materials: the Chern insulator and graphene.

In the second part of this thesis we study the critical signatures of Weyl semimetals, showing how these materials need to break either inversion symmetry or time-reversal symmetry to exist, and some direct consequences of the electronic structure such as the appearance of an anomalous quantum Hall effect and the chiral anomaly. In addition, we review the experimental discoveries of the last years.

In the third part of the thesis, we shift focus towards quantum transport, more specifically in the Landauer coherent approach to transport. We deduce the origin of the Landauer-Büttiker formula and elucidate why a multiterminal response is needed to measure non-local transport properties in a material. The crucial part of this section is that it provides us with the mathematical tools for calculating transport responses on a Weyl Semimetal.

The final chapter consists of the original research carried on this thesis. Here, we report on atomistic simulations of the dc conductance and quantum Hall response of a minimal Weyl semimetal. By using scattering theory, we show that a quantized Hall conductance with a non-vanishing longitudinal conductance emerges associated with the Fermi arc surface states with remarkable robustness to high concentrations of defects in the system. Additionally, we predict that a slab of a Weyl semimetal with broken time-reversal symmetry bears persistent currents entirely determined by the system size and the lattice parameters.

Agradecimientos

Quisiera agradecer a Jenni, Tamidim, Tami, Pipón, Vodka, Arturo, Hugo, Renata, Susy, Leslie, Daniel, Fabio, Maiguel, Fran, Rho, Nico, Feña, Tebi, Kito, Tania, Walter, Juanca, Caro, Josu, Guille, Archie, Eva, JG, Marcelo, Matus, Ariel, Atenas, Karpi, Ivana, Beba, Carlos, Leo, Jo, Mono, Felipe, Luis, Álvaro, Andy, Rodrigo, Néstor, Carla y Marcos. Amigas y amigos, profesora y profesores que me han acompañado y guiado en esta etapa del Magíster, ya sea desarrollando investigación, con consejos y conversas, tocando guitarra, fumando, o tomándose sus chelas y vinitos. Mucho amor para todes.

Una mención especial a mi familia, que siempre me han apoyado y motivado para que termine este postgrado, y que siga camino adelante con mi futuro.

Contents

List of Figures

Chapter 1

Introduction

Topological but gapless, Weyl semimetals [1, 2] challenge our physical intuition with striking properties, thereby constituting a new paradigm in the physics of topological quantum matter. One of their distinctive features is the presence of Weyl nodes, discrete points in the three-dimensional (3D) Brillouin zone where the valence and conduction bands meet forming a 3D analog of graphene. Unlike the Dirac points in graphene, Weyl nodes are non-degenerate, and a perturbation does not gap the system, it only shifts the Weyl nodes in k-space [3]. Interestingly, the existence of Weyl nodes in the sample's bulk dispersion, which appears in pairs of opposite chirality acting as Berry phase monopoles, can be tied to the presence of Fermi arc surface states at the boundary of a finite system. Control over the exotic electronic properties of a Weyl semimetal is expected to lead to the development of novel devices. In particular, high-temperature quantum devices are envisioned to take advantage of the topological protection of their states. Superconducting Weyl semimetals, expected to host unique forms of Majorana fermions, are likely to aid in the development of quantum information devices. [4–8]

Fueled by the experimental observation of Weyl semimetals in recent years [9–11], a plethora of different flavors is now known to exist [12], and there is a fierce competition to unveil them in the laboratory. For Weyl semimetals to exist, either inversion symmetry (IS) or time-reversal symmetry (TRS) must be broken. Although almost all of the experimental realizations correspond to those of the first type, this year the first experimental realization of one of the latter species has been made [13]. While most experiments rely heavily on probing the electronic dispersion through angle-resolved photoemission spectroscopy (ARPES), transport experiments are also expected to provide for valuable information [14, 15]. In the bulk of the semimetal, the conductivity tensor is predicted to be anisotropic and, depending on the crystal symmetry, a giant anomalous Hall effect may arise [16] ($\sigma_{yz} = \frac{e^2}{2\pi h}(k_+ - k_-)$, with $k_+ - k_-$ being the momentum separation between the Weyl Nodes.)

In spite of the intense research, with few exceptions [17–19], most studies have focused on the bulk rather than the surface transport properties of Weyl semimetals [16, 20, 21]. Besides being an easier to access property than its bulk counterpart, the transport response measured at the surface may guard new hallmarks of the Weyl semimetal phase. Theoretical simulations may help to unveil them while clarifying many interesting aspects that are unique to this topological phase. For example, in contrast to topological insulators, the bulk states in Weyl Semimetals are expected to play a role in transport [22]. But the complex electronic structure of many Weyl semimetals sometimes featuring dozens of Weyl nodes poses an obstacle in this young field. Studying a simple "hydrogen-like" model of a Weyl semimetal is, therefore, a first necessary step.

In this thesis, we begin by explaining all the theoretical background needed to approach the problem in question. In the following three chapters we will show what is topology in condensed matter systems, what are and what properties do Weyl semimetals have, and what is the Landauer-Büttiker formula and how it is useful to calculate transport properties of quantum systems.

Afterward comes the bulk of the carried research. Here we report on the electronic and transport properties of a minimal Weyl semimetal with only two Weyl nodes. This minimal model, which requires broken

time-reversal symmetry, is used as a playground for the study of the multiterminal conductance at the surface of a finite slab within a coherent approach. To such end, we combine a scattering formulation of transport with a tight-binding model. Our simulations show that associated with the Fermi arc surface states, there is a nearly quantized Hall conductance which remains robust to imperfections and defects.

Furthermore, and unlike to Chern insulators, the Hall response has a non-vanishing longitudinal conductance. These two observations, the deviations of the Hall conductance from perfect quantization and the non-vanishing longitudinal conductance, are a consequence of the unavoidable leak of the surface states into the bulk. We also test the topological nature of our quantized conductance results by adding random lattice defects and find that they remain robust at concentrations of the order of 25% which is remarkably higher than what has been previously reported on 2D topological systems [23].

Interestingly, our results also show that a slab of a Weyl semimetal can bear persistent currents even in the absence of a magnetic field. These currents are governed by the system size and the intrinsic time-reversal symmetry breaking lattice parameters and can explain why there is no surface transport in the direction perpendicular to the Fermi arcs.

Being impervious to disorder, the transport properties of the surface states of a Weyl semimetal have extraordinary potential in applications in nanotechnological devices. In this way, the calculations done in this thesis provide the motivation and are the starting point of new simulations required to elucidate the role of finite geometries upon the transport properties of more complex Weyl semimetals that have a real analog in the laboratory.

Chapter 2

Topological Band Theory

The title of this thesis is *Transport Properties of Weyl Semimetals*. To understand the research carried in this thesis, we need to ask ourselves:

1. What are Weyl semimetals?
2. What do we mean when we talk about electron transport?

To begin to answer the first of these questions, we need to introduce the theoretical background associated with topological band theory. We will review only the most general aspects in order to make this thesis self-contained. The reader interested in a more in-depth discussion can refer to [24–28].

2.1 Topological Band Theory

Topology is a branch of mathematics that deals with the geometric properties of objects that are invariant to smooth transformations [29]. The most straightforward example of objects to imagine are closed two-dimensional surfaces; we can imagine a sphere that can be smoothly changed into many other objects, such as a disk or a bowl. But there are other objects that the sphere cannot be deformed continuously onto such as a doughnut or a mug, since they contain holes on their surface. These two classes of objects are topologically distinct, and to differentiate them, we can define a topological invariant in virtue of the Gauss-Bonnet theorem called the Euler characteristic.

The Euler characteristic χ is defined as [29]:

$$\chi = \frac{1}{2\pi} \int_S K dA \tag{2.1}$$

where K is the Gaussian curvature of our object of interest. In particular, for the first class of objects in our example, the sphere and the disk, $\chi = 2$, while for the other class of objects, the doughnut and the mug, $\chi = 0$. We see that χ discriminates objects of different topological classes.

Naturally, we ask ourselves, how does topology play a role in the context of electrons in solids and band theory? We will see that for a band system we can define topological invariants of a similar nature to the Euler characteristic.

Let's begin making some assumptions. First, let's suppose we have electrons moving on the atoms of a crystalline lattice. Then, there is translational invariance, and the k-space becomes periodic in virtue of

the Bloch's theorem. Consequently, band structures arise since the energy of the electrons now becomes a function of the crystal momentum.

In the second place, let's assume that the bands have an energy gap. Since the bands are separated from each other, each one of them defines a target bundle on k-space that is a T_2 torus for the bidimensional case. We'll now see that the mapping of the bandstructure onto the bundle may or may not be topological, and that information is encoded in the eigenfunctions of the Bloch Hamiltonian.

Let's suppose we have a Hamiltonian that evolutions adiabatically due to a time-varying parameter that, in particular for this case, can be the crystal momentum k. The eigenfunctions satisfy:

$$H(\mathbf{k})|u(\mathbf{k})\rangle = E_{\mathbf{k}}|u(\mathbf{k})\rangle \tag{2.2}$$

The previous equation determines the Bloch eigenfunctions up to an arbitrary phase $e^{i\phi(\mathbf{k})}$.

Let's define the Berry connection as:

$$\mathbf{A} = -i\langle u(\mathbf{k})|\nabla_{\mathbf{k}}|u(\mathbf{k})\rangle \tag{2.3}$$

and the Berry phase as,

$$\gamma_C = \int_C \mathbf{A}\cdot d\mathbf{k} \tag{2.4}$$

Let's try to elucidate what physical meaning do the Berry connection and Berry phase carry. We see that under the gauge transformation $|u(\mathbf{k})\rangle \to e^{i\phi(\mathbf{k})}|u(\mathbf{k})\rangle$, $\mathbf{A}$ transforms as:

$$\begin{aligned}\mathbf{A} &\to -ie^{-i\phi(\mathbf{k})}\langle u(\mathbf{k})|\nabla_{\mathbf{k}}\Big(e^{i\phi(\mathbf{k})}|u(\mathbf{k})\rangle\Big)\\ &= -i\langle u(\mathbf{k})|\nabla_{\mathbf{k}}|u(\mathbf{k})\rangle + \nabla_{\mathbf{k}}\phi\\ &= \mathbf{A} + \nabla_{\mathbf{k}}\phi\end{aligned} \tag{2.5}$$

This result is reminiscent of the electromagnetic gauge freedom in the vector potential, and that is because the underlying symmetry of the quantum wavefunctions is $U(1)$. Then, we can think of the Berry connection as the gauge field for this $U(1)$ symmetry. $\mathbf{A}$ is not gauge invariant, but just as it happens in electromagnetism, the associated magnetic flux must be gauge invariant. The analog of the magnetic field in electromagnetism is:

$$\mathcal{F} = \nabla_{\mathbf{k}}\times\mathbf{A} \tag{2.6}$$

We can check that $\mathcal{F}$ is gauge-invariant:

$$\begin{aligned}\mathcal{F} &\to \nabla_{\mathbf{k}}\times(\mathbf{A}+\nabla_{\mathbf{k}}\phi)\\ &= \mathcal{F}\end{aligned} \tag{2.7}$$

since $\nabla\times\nabla\phi = 0$. From here onwards, we'll drop the $\mathbf{k}$ from the $\nabla_{\mathbf{k}}$.

Written in function of the Berry curvature, the Berry phase is:

$$\begin{aligned}\gamma_C &= \int_C \mathbf{A} \cdot d\mathbf{k} \\ &= \int_S (\nabla \times \mathbf{A}) \ d^2\mathbf{k} \\ &= \int_S \mathcal{F} \ d^2k\end{aligned} \tag{2.8}$$

Since the number of magnetic monopoles in $\vec{k}$-space is

$$n = \frac{1}{2\pi} \int_S \mathcal{F} \ d^2k \tag{2.9}$$

Then, the Berry phase is just 2π the number of monopoles in magnetic space:

$$\gamma_C = 2\pi n \tag{2.10}$$

We have now elucidated the physical significance of the Berry phase. We will now connect the emergence of magnetic monopoles in $\vec{k}$-space to an ill-defined gauge of the eigenstates of the system.

For simplicity, let's assume a two-level system. The Hamiltonian can be expressed as:

$$H(\mathbf{k}) = \vec{d}(\mathbf{k}) \cdot \vec{\sigma} \tag{2.11}$$

where we have ignored the energy shift $\epsilon_0 I$ since it's irrelevant. The vector $\vec{d}$ can be parametrized in spherical coordinates:

$$\vec{d}(\mathbf{k}) = d(\sin\theta\cos\psi, \sin\theta\sin\psi, \cos\theta) \tag{2.12}$$

where (θ, ψ) are functions of $\mathbf{k}$. With this mapping, the eigenstates of the system in a particular gauge are:

$$|+\rangle = \begin{pmatrix} \cos(\theta/2)e^{i\psi} \\ \sin(\theta/2) \end{pmatrix} \quad |-\rangle = \begin{pmatrix} \sin(\theta/2)e^{i\psi} \\ -\cos(\theta/2) \end{pmatrix} \tag{2.13}$$

Examining the eigenstates, we can see that at $\theta = 0$, the eigenfunctions become ill-defined since the eigenstates stop being single-valued. If we take another gauge choice, for example, there will always exist one angle where the eigenstates are no longer single-valued. We will now show a case where if the Hamiltonian reaches the parameter space where the gauge is not well defined in its adiabatic, then the system is equivalent as having a magnetic monopole in $\mathbf{k}$.

Let's choose as an example $d(\mathbf{k}) = \mathbf{k}$. Since the vector $\vec{d}$ will roam the entire Bloch sphere for every value of $\mathbf{k}$, it will pick every value of θ available and pass through the ill-defined value for the gauge. The Berry curvature must correspond then to a magnetic monopole one if we calculate it.

Let's focus on the negative energy eigenstate (the positive one analysis is analogous). The Berry connection components are:

$$\begin{aligned}A_\theta &= -i\langle -|\partial_\theta|-\rangle \\ &= 0\end{aligned} \tag{2.14}$$

$$\begin{aligned} A_\psi &= -i\langle -|\partial_\psi|-\rangle \\ &= \sin^2(\theta/2) \end{aligned} \tag{2.15}$$

So:

$$\mathbf{A} = \sin^2(\theta/2)\hat{\psi} \tag{2.16}$$

Then, the Berry curvature is:

$$\begin{aligned} \mathcal{F} &= \nabla \times \mathbf{A} \\ &= \frac{1}{r\sin\theta}\partial_\theta(A_\psi \sin\theta)\hat{r} \\ &= \frac{\hat{r}}{2r} \end{aligned} \tag{2.17}$$

This result is the field generated by a magnetic monopole of charge $1/2$. Shall we have chosen the opposite eigenstate, we had gotten a magnetic monopole of charge $-1/2$. The main conclusion of this section is that singularities in parameter space act as drains and sources of Berry flux, and thus, of a non-trivial Berry phase.

More generally [30], the Berry phase is

$$\gamma_C = \frac{\Omega}{2} \tag{2.18}$$

where Ω is the solid angle swept out by the vector $\hat{d}$ on the Bloch sphere and the Berry curvature is

$$\begin{aligned} \mathcal{F} &= \frac{1}{2}\epsilon_{ij}\hat{d}\cdot(\partial_i\hat{d}\times\partial_j\hat{d}) \\ &= 2\pi\nu \end{aligned} \tag{2.19}$$

Thus, the Berry curvature is the solid angle per unit area in $\mathbf{k}$ space. These expressions give an account of the connection between the Berry phase and the geometry of the eigenfunctions on the Bloch sphere: The Berry curvature is just 2π times the winding number ν of the vector $\hat{d}$ around the sphere. In the context of topological band theory, we call ν the Chern number and identify it as a topological invariant. A null Chern number represents a system topologically trivial while a non-zero Chern number represents a topologically non-trivial system. Since the parameter space is periodic in $\mathbf{k}$ space, the vector $\hat{d}$ must end where it begins in its wrapping. Therefore, the Chern number is always quantized in integers.

The most important thing is that for two systems that have the same topological nature (hence, the same Chern number), we can continuously deform the eigenstates of one system onto the another, but for systems that have different topological nature, it's impossible to perform a continuous deformation unless we close the energy gap separating the bandstructure. In the context of topological band theory, we call systems with a non zero Chern number topologically protected, because external perturbations only deform the eigenstates onto another set that is topologically equivalent and therefore, that has the same physical observable properties. Only when the disturbance is large enough to close the gap, the system may change its physical properties.

2.2 Integer Quantum Hall Effect

One of the key signatures of a topological system in 2D is that its edge states are reminiscent of those in an integer quantum Hall effect [31, 32]. In many cases, this can happen in the absence of an external magnetic field signaling the appearance of an anomalous quantum Hall effect.

The filling factor in the integer quantum Hall effect was shown to be the Chern number of topological systems in the seminal paper by Thouless, Kohmoto, Nightingale and des Nijs, where they called this topological invariant the TKKN invariant [33]. In the next section, we will follow closely the derivation made in [34].

Let's assume we have a two-dimensional two-band gapped Hamiltonian. As we have seen, we can express it as $H = \sum_k H_k$ with $H_k = \epsilon(\mathbf{k})\sigma_0 + \vec{d}\cdot\vec{\sigma}$ and the eigenenergies being $E_\pm = \epsilon(\mathbf{k}) \pm d(\mathbf{k})$. Using the Kubo formula, the Hall conductance is [35, 36]

$$\sigma_{xy} = \lim_{\omega\to 0} \frac{i}{\omega} Q_{xy}(w + i\delta) \tag{2.20}$$

with Q_{xy} the current-current response function

$$Q_{xy}(i\nu_m) = \frac{1}{\Omega\beta} \sum_{\mathbf{k},n} Tr[J_x(\mathbf{k})G(\mathbf{k}, i(\omega_n + \nu_m))J_y(\mathbf{k})G(\mathbf{k}, i\omega_n)] \tag{2.21}$$

where J is the current operator given by

$$\begin{aligned} J_i(\mathbf{k}) &= \frac{\partial H_k}{\partial k_i} \\ &= \frac{\partial \epsilon(\mathbf{k})}{\partial k_i} + \frac{\partial d_\alpha(\mathbf{k})}{\partial k_i}\sigma^\alpha \end{aligned} \tag{2.22}$$

and $G(\mathbf{k}, i\omega_n)$ is the Matsubara Green function.

Since the Hamiltonian is a 2×2 matrix, the Green function can be calculated.

$$\begin{aligned} G(\mathbf{k}, i\omega_n) &= [i\omega_n - H(\mathbf{k})]^{-1} \\ &= [(i\omega_n - \epsilon(\vec{k}))\sigma_0 - d_\alpha\sigma^\alpha]^{-1} \\ &= \frac{1}{det((i\omega_n - \epsilon(\vec{k}))\sigma_0 - d_\alpha\sigma^\alpha)}[(i\omega_n - \epsilon(\vec{k}))\sigma_0 + d_\alpha\sigma^\alpha] \\ &= \frac{(i\omega_n - \epsilon(\vec{k}))\sigma_0 + d_\alpha\sigma^\alpha}{(i\omega_n - \epsilon(\vec{k}))^2 - d^2} \\ &= \frac{1}{2}\Big(\frac{\sigma_0 - \hat{d}_\alpha\sigma^\alpha}{i\omega_n - \epsilon(\vec{k}) + d} + \frac{\sigma_0 + \hat{d}_\alpha\sigma^\alpha}{i\omega_n - \epsilon(\vec{k}) + d}\Big) \\ &= \frac{1}{2}\Big(\frac{\sigma_0 - \hat{d}_\alpha\sigma^\alpha}{i\omega_n - E_-} + \frac{\sigma_0 + \hat{d}_\alpha\sigma^\alpha}{i\omega_n - E_+}\Big) \\ &= \frac{P_+}{i\omega_n - E_+} + \frac{P_-}{i\omega_n - E_-} \\ &= \sum_\mu \frac{P_\mu}{i\omega_n - E_\mu} \end{aligned} \tag{2.23}$$

where $P_\mu = \frac{1 \pm \hat{d}_\alpha(\mathbf{k})\sigma^\alpha}{2}$ and μ can take the values $\mu = +$ or $\mu = -$. Then, the response function is:

$$Q_{xy}(i\nu_m) = \frac{1}{\Omega\beta} \sum_{\mathbf{k}n\mu\mu'} \frac{Tr[J_x P_\mu J_y P_{\mu'}]}{[i(\omega_n + \nu_m) - E_\mu][i\omega_n - E_{\mu'}]} \tag{2.24}$$

One of the summations is a Matsubara frequency summation which we can perform directly:

$$\begin{aligned} \sum_n \frac{1}{[i(\omega_n + \nu_m) - E_\mu][i\omega_n - E_{\mu'}]} &= Res\Big(\frac{1}{[z + i\nu_m - E_\mu][z - E_{\mu'}]} \frac{\beta}{e^{\beta\mu} - 1}\Big) \\ &= \frac{\beta}{E_\mu - E_{\mu'} + i\nu_m}(n_\mu - n_{\mu'}) \end{aligned} \tag{2.25}$$

Therefore, the response function is:

$$Q_{xy}(i\nu_m) = \frac{1}{\Omega} \sum_{\mathbf{k}\mu\mu'} \frac{Tr[J_x P_\mu J_y P_{\mu'}]}{i\nu_m - E_{\mu'} + E_\mu}(n_\mu - n_{\mu'}) \tag{2.26}$$

Using this on equation 2.20:

$$\begin{aligned} \sigma_{xy} &= \lim_{\omega\to 0} \frac{i}{\omega} Q_{xy}(w + i\delta) \\ &= \lim_{\omega\to 0} \frac{i}{\omega\Omega} \sum_{\mathbf{k}\mu\mu'} \frac{Tr[J_x P_\mu J_y P_{\mu'}]}{\omega + i\delta - E_{\mu'} + E_\mu}(n_\mu - n_{\mu'}) \end{aligned} \tag{2.27}$$

Expanding around $\omega = 0$ we have:

$$\frac{1}{\omega + i\delta - E_{\mu'} + E_\mu} = \frac{1}{i\delta - E'_\mu + E_\mu} - \frac{\omega}{(i\delta - E_{\mu'} + E_\mu)^2} + \mathcal{O}(\omega^2) \tag{2.28}$$

Therefore:

$$\sigma_{xy} = \lim_{\omega\to 0} \frac{i}{\omega\Omega} \sum_{\mathbf{k}\mu\mu'} \Big(\frac{Tr[J_x P_\mu J_y P_{\mu'}]}{i\delta - E_{\mu'} + E_\mu}(n_\mu - n_{\mu'}) - \omega \frac{Tr[J_x P_\mu J_y P_{\mu'}]}{(i\delta - E_{\mu'} + E_\mu)^2}(n_\mu - n_{\mu'}) + \mathcal{O}(\omega^2) \Big) \tag{2.29}$$

We will now show that the zeroth-order term of the expansion is zero:

$$\begin{aligned} \sum_{\mu\mu'} \frac{Tr[J_x P_\mu J_y P_{\mu'}]}{i\delta - E_{\mu'} + E_\mu}(n_\mu - n_{\mu'}) &= \frac{Tr[J_x P_+ J_y P_-]}{i\delta - E_- + E_+}(n_+ - n_-) + \frac{Tr[J_x P_- J_y P_+]}{i\delta - E_+ + E_-}(n_- - n_+) \\ &\quad + \frac{Tr[J_x P_+ J_y P_+]}{i\delta}(n_+ - n_+) + \frac{Tr[J_x P_- J_y P_-]}{i\delta}(n_- - n_-) \\ &= \frac{Tr[J_x P_+ J_y P_-]}{i\delta - E_- + E_+}(n_+ - n_-) + \frac{Tr[J_x P_- J_y P_+]}{i\delta - E_+ + E_-}(n_- - n_+) \end{aligned} \tag{2.30}$$

Using that $E_+ - E_- = 2d$:

$$\sum_{\mu\mu'} \frac{Tr[J_x P_\mu J_y P_{\mu'}]}{i\delta - E_{\mu'} + E_\mu}(n_\mu - n_{\mu'}) = \frac{Tr[J_x P_+ J_y P_-]}{i\delta + 2d}(n_+ - n_-) + \frac{Tr[J_x P_- J_y P_+]}{i\delta - 2d}(n_- - n_+) \tag{2.31}$$
$$= \frac{n_+ - n_-}{4d^2 - \delta^2}((i\delta - 2d)Tr[J_x P_+ J_y P_-] - (i\delta + 2d)Tr[J_x P_- J_y P_+])$$

Using that δ is small, we can take $\delta = 0$:

$$\sum_{\mu\mu'} \frac{Tr[J_x P_\mu J_y P_{\mu'}]}{i\delta - E_{\mu'} + E_\mu}(n_\mu - n_{\mu'}) = -\frac{n_+ - n_-}{2d}(Tr[J_x P_+ J_y P_-] + Tr[J_x P_- J_y P_+]) \tag{2.32}$$

Using that all the P_μ and J_μ are hermitian:

$$\sum_{\mu\mu'} \frac{Tr[J_x P_\mu J_y P_{\mu'}]}{i\delta - E_{\mu'} + E_\mu}(n_\mu - n_{\mu'}) = -\frac{n_+ - n_-}{2d}(Tr[J_x P_+ J_y P_-] + h.c.) \tag{2.33}$$

Let's calculate the trace in more detail:

$$Tr[J_x P_+ J_y P_-] = \frac{1}{4} Tr[(\partial_{k_x}\epsilon + \partial_{k_x} d_\alpha \sigma^\alpha)(1 + \hat{d}_\beta \sigma^\beta)(\partial_{k_y}\epsilon + \partial_{k_y} d_\gamma \sigma^\gamma)(1 - \hat{d}_\delta \sigma^\delta)] \tag{2.34}$$

Using that the trace of the Pauli matrices is:

$$Tr[\sigma_\alpha \sigma_\beta \sigma_\gamma] = 2i\epsilon_{\alpha\beta\gamma} \tag{2.35}$$

and all other combinations are null, we have

$$\begin{aligned} Tr[J_x P_+ J_y P_-] &= \frac{1}{4}\Big[-(\partial_{k_x}\epsilon)\hat{d}_\beta(\partial_{k_y} d_\gamma)\hat{d}_\delta Tr[\sigma^\beta\sigma^\gamma\sigma^\delta] - (\partial_{k_x} d_\alpha)(\partial_{k_y} d_\gamma)\hat{d}_\delta Tr[\sigma^\alpha\sigma^\gamma\sigma^\delta] \\ &\quad - (\partial_{k_x} d_\alpha)\hat{d}_\beta(\partial_{k_y}\epsilon)\hat{d}_\delta Tr[\sigma^\alpha\sigma^\beta\sigma^\delta] + (\partial_{k_x} d_\alpha)\hat{d}_\beta(\partial_{k_y} d_\gamma)Tr[\sigma^\alpha\sigma^\beta\sigma^\gamma]\Big] \\ &= \frac{i}{2}\Big[-(\partial_{k_x}\epsilon)\hat{d}_\beta(\partial_{k_y} d_\gamma)\hat{d}_\delta \epsilon^{\beta\gamma\delta} - (\partial_{k_x} d_\alpha)(\partial_{k_y} d_\gamma)\hat{d}_\delta \epsilon^{\alpha\gamma\delta} \\ &\quad - (\partial_{k_x} d_\alpha)\hat{d}_\beta(\partial_{k_y}\epsilon)\hat{d}_\delta \epsilon^{\alpha\beta\delta} + (\partial_{k_x} d_\alpha)\hat{d}_\beta(\partial_{k_y} d_\gamma)\epsilon^{\alpha\beta\gamma}\Big] \\ &= \frac{i}{2}\Big[-(\partial_{k_x}\epsilon)\hat{d}_\alpha(\partial_{k_y} d_\beta)\hat{d}_\gamma - (\partial_{k_x} d_\alpha)(\partial_{k_y} d_\beta)\hat{d}_\gamma \\ &\quad - (\partial_{k_x} d_\alpha)\hat{d}_\beta(\partial_{k_y}\epsilon)\hat{d}_\gamma + (\partial_{k_x} d_\alpha)\hat{d}_\beta(\partial_{k_y} d_\gamma)\Big]\epsilon^{\alpha\beta\gamma} \end{aligned} \tag{2.36}$$

For the first and third term, we have a product between a symmetric and an antisymmetric term, therefore they are null. The second and fourth terms are equal rearranging indexes.

$$Tr[J_x P_+ J_y P_-] = -\frac{i}{2}(\partial_{k_x} d_\alpha)(\partial_{k_y} d_\beta)\hat{d}_\gamma \epsilon^{\alpha\beta\gamma} \tag{2.37}$$

Since $\epsilon(\vec{k})$ and all d_μ are real, the trace is purely imaginary. Therefore, in equation 2.33, the sum of traces gives zero:

$$\begin{aligned}\sum_{\mu\mu'} \frac{Tr[J_x P_\mu J_y P_{\mu'}]}{i\delta - E_{\mu'} + E_\mu}(n_\mu - n_{\mu'}) &= -\frac{n_+ - n_-}{2d}(Tr[J_x P_+ J_y P_-] + h.c.) \\ &= 0\end{aligned} \tag{2.38}$$

Now in the Hall conductance we can take the limit of 2.29:

$$\begin{aligned}\sigma_{xy} &= \lim_{\omega\to 0}\frac{i}{\omega\Omega}\sum_{\mathbf{k}\mu\mu'}\Big(\frac{Tr[J_x P_\mu J_y P_{\mu'}]}{i\delta - E_{\mu'} + E_\mu}(n_\mu - n_{\mu'}) - \omega\frac{Tr[J_x P_\mu J_y P_{\mu'}]}{(i\delta - E_{\mu'} + E_\mu)^2}(n_\mu - n_{\mu'}) + \mathcal{O}(\omega^2)\Big) \\ &= \lim_{\omega\to 0}\frac{i}{\omega\Omega}\sum_{\mathbf{k}\mu\mu'}\Big(-\omega\frac{Tr[J_x P_\mu J_y P_{\mu'}]}{(i\delta - E_{\mu'} + E_\mu)^2}(n_\mu - n_{\mu'}) + \mathcal{O}(\omega^2)\Big) \\ &= -\frac{i}{\Omega}\sum_{\mathbf{k}\mu\mu'}\frac{Tr[J_x P_\mu J_y P_{\mu'}]}{(i\delta - E_{\mu'} + E_\mu)^2}(n_\mu - n_{\mu'})\end{aligned} \tag{2.39}$$

Again, we can use $\delta = 0$:

$$\begin{aligned}\sigma_{xy} &= -\frac{i}{\Omega}\sum_{\mathbf{k}\mu\mu'}\frac{Tr[J_x P_\mu J_y P_{\mu'}]}{(E_\mu - E_{\mu'})^2}(n_\mu - n_{\mu'}) \\ &= -\frac{i}{\Omega}\sum_{\mathbf{k}}\Big(\frac{Tr[J_x P_+ J_y P_-]}{(E_+ - E_-)^2}(n_+ - n_-) + \frac{Tr[J_x P_- J_y P_+]}{(E_+ - E_-)^2}(n_- - n_+)\Big)\end{aligned} \tag{2.40}$$

But $(E_+ - E_-)^2 = 4d^2$. Then:

$$\sigma_{xy} = -\frac{i}{4\Omega}\sum_{\vec{k}}\frac{n_+ - n_-}{d^2}(Tr[J_x P_+ J_y P_-] - Tr[J_x P_- J_y P_+]) \tag{2.41}$$

Again, we can use that all the P_μ and J_μ are hermitian:

$$\sigma_{xy} = -\frac{i}{4\Omega}\sum_{\vec{k}}\frac{n_+ - n_-}{d^2}(Tr[J_x P_+ J_y P_-] - h.c.) \tag{2.42}$$

Substracting the hermitian conjugate of 2.37, we have:

$$\sigma_{xy} = -\frac{1}{2\Omega}\sum_{\mathbf{k}}\Big(\frac{\partial d_\alpha}{\partial k_x}\frac{\partial d_\beta}{\partial k_y}d_\gamma\epsilon^{\alpha\beta\gamma}\Big)(n_- - n_+) \tag{2.43}$$

At zero temperature, $n_- = 1$ and $n_+ = 0$

$$\begin{aligned}\sigma_{xy} &= -\frac{1}{2\Omega}\sum_{\mathbf{k}}\frac{\partial d_\alpha}{\partial k_x}\frac{\partial d_\beta}{\partial k_y}d_\gamma\epsilon^{\alpha\beta\gamma} \\ &= -\frac{1}{2\Omega}\sum_{\mathbf{k}}\Big(\frac{\partial\hat{d}}{\partial k_x}\times\frac{\partial\hat{d}}{\partial k_y}\Big)\cdot\hat{d}\end{aligned} \tag{2.44}$$

Taking the thermodynamic limit:

$$\sigma_{xy} = \frac{e^2}{4\pi h} \int d^2k \Big(\frac{\partial \hat{d}}{\partial k_x} \times \frac{\partial \hat{d}}{\partial k_y} \Big) \cdot \hat{d} \tag{2.45}$$

Recalling equation 2.19, we conclude that

$$\sigma_{xy} = \frac{e^2}{h} \nu \tag{2.46}$$

where ν is the Chern number of the system.

Thus, we have concluded that the filling factor in the integer quantum Hall effect is connected to the topology of the band system, and moreover, the Hall conductivity of a system is also a topological invariant provided the system has a non-trivial topological band structure. This is the first encounter of the bulk-edge correspondence; the topological properties of the bulk Hamiltonian are connected to properties that occur on the edge of a finite sample of the same system.

It is essential to remind ourselves that the protected quantity is the Hall conductivity, which is not an observable quantity. The observable quantity in an experiment is the Hall conductance, which is by no means topologically protected and could deviate from quantization due to finite size effects such as the geometry of the sample or leads position in the experiment. This remark will be of importance in the analysis of the later results.

2.3 Topological Insulators

To begin this section, let's prelude the explanation of topological insulators by showing that massive bidimensional Dirac fermions on a lattice are topologically non-trivial systems. The results in this section follow closely [24] and [37].

Massive Dirac fermions satisfy the Dirac equation:

$$i\hbar\gamma^\mu \partial_\mu \psi - m\psi = 0 \tag{2.47}$$

For a electrons confined in a continuum bidimensional system, the Hamiltonian takes a simpler form using the Pauli matrices:

$$H(\vec{k}) = k_x \sigma_x + k_y \sigma_y + m\sigma_z \tag{2.48}$$

Therefore, for this Hamiltonian we have $E(\vec{k}) = \pm\sqrt{k^2 + m^2}$ and $\vec{d} = (k_x, k_y, m)$. Plugging the latter into 2.19 we obtain:

$$\begin{aligned} F_{xy} &= \frac{1}{2d^3} \epsilon^{abc} d_a \partial_{k_x} d_b \partial_{k_y} d_c \\ &= \frac{m}{2d^3} \epsilon^{ij} \partial_{k_x} k_i \partial_{k_y} k_j \\ &= \frac{1}{2} \frac{m}{(m^2 + k^2)^{3/2}} \end{aligned} \tag{2.49}$$

In virtue of equations 2.19 and 2.46, we have:

$$\begin{aligned}\sigma_{xy}^{continuum} &= \frac{e^2}{h}\frac{1}{2\pi}\int d^2k F_{xy} \\ &= \frac{e^2}{2h}\int_0^\infty \frac{mk}{(m^2+k^2)^{3/2}}dk \\ &= \frac{e^2}{h}\frac{sgn(m)}{2}\end{aligned} \tag{2.50}$$

Therefore, continuum Dirac fermions confined to two dimensions have a half-integer quantized hall conductivity. To extend our analysis to the case of the fermions on a lattice we have to consider that our conductance result is no longer valid since the fermions can't have infinite bandwidth (due to the discretization of the lattice), and therefore the band spectrum $E(\vec{k}) = \pm(k^2+m^2)^{1/2}$ can no longer represent a valid theory on a lattice: the bands must bend over at some point on the Brillouin zone.

Massive Dirac fermions on a lattice can be realized by considering a generalization of the Hamiltonian 2.48:

$$H(\mathbf{k}) = \epsilon_0(\mathbf{k})\mathbb{I} + \vec{d}(\mathbf{k})\cdot\vec{\sigma} \tag{2.51}$$

This hamiltonian has a band dispersion of $E(\mathbf{k}) = \epsilon_0(\mathbf{k}) \pm |\vec{d}(\mathbf{k})|$. In order to realize massive bidimensional Dirac fermions, we require the existence of at least one point $\mathbf{K}$ in the dispersion where the low energy excitations correspond to these particles:

$$H(\mathbf{K}) \approx k_x\sigma_x + k_y\sigma_y + M\sigma_z \tag{2.52}$$

Then, we have an electronic spectrum that does not have the infinite bandwidth problem but that locally at the point $\mathbf{K}$ has massive Dirac particle excitations. In order to elucidate if there are topological properties associated with these fermions, we need to fix the mass term in the general hamiltonian. For spinless particles, there are four different mass choices that give out the required low energy excitations; we will analyze the Haldane mass term that results in topological properties.

A Haldane mass corresponds to a choice of functions $\epsilon_0(\mathbf{k})$ and $\vec{d}(\mathbf{k})$ that break time-reversal symmetry on the hamiltonian but preserve the spatial inversion symmetry. Since the latter symmetry is preserved, the existence of a point $\mathbf{K}$ on the Brillouin zone where the low energy excitations correspond to massive Dirac fermions (which is called a valley), imply that there also must exist another valley at $-\mathbf{K}$. In addition, the invariance under inversion symmetry implies that the function $d_z(\mathbf{k})$ accompanying the Pauli matrix σ_z must satisfy $d_z(\mathbf{k}) = -d_z(-\mathbf{k})$. In particular, this in turn, implies that each pair of valleys must have equal masses of opposing signs.

Let's assign the variable $\xi = \pm 1$ to differentiate the signs of the two valleys; we have for the valley ξ the following low-energy Hamiltonian:

$$H^\xi \approx k_x\sigma_x + k_y\sigma_y + M\xi\sigma_z \tag{2.53}$$

Recalling equations 2.49 and 2.50 we have for each valley:

$$F_{xy}^\xi = \frac{1}{2}\frac{m\xi}{(m^2+k^2)^{3/2}} \tag{2.54}$$

$$\begin{aligned}\sigma_{xy}^{\xi} &= \frac{e^2}{h}\frac{1}{2\pi}\int d^2k F_{xy}^{\xi} \\ &= \frac{e^2}{h}\frac{\xi sgn(\xi m)}{2}\end{aligned} \tag{2.55}$$

Without loss of generality let's take $m > 0$. Then, the total contribution to the Hall conductivity for both valleys is:

$$\begin{aligned}\sigma_{xy} &= \sigma_{xy}^{+1} + \sigma_{xy}^{-1} \\ &= \frac{e^2}{2h} - \Big(-\frac{e^2}{2h}\Big) \\ &= \frac{e^2}{h}\end{aligned} \tag{2.56}$$

This signals the appearance of an IQHE, which we have already seen, is connected to topological properties on the band spectrum. In particular, for the case of a pair of valleys, the Chern number ν of the system takes the non-trivial value of 1. It is important to note that varying the sign of the mass term from positive to negative shifts the energy of each valley, which in turn generates a band inversion of the energy spectrum. In-between the varying of the sign of the mass, m is equal to zero, and the system becomes gapless, signaling a type of topological transition. In general, we can associate the appearance of topology in a gapped band system with the inversion of the energy bands.

Now we are ready to introduce topological insulators. A topological insulator is a gapped band system defined on a lattice, where the low energy excitations behave as two dimensional massive Dirac fermions with topologically non-trivial associated edge states. Let's study in detail the most basic topological insulator, the Chern Insulator, whose origin is in the square discretization of the Dirac hamiltonian presented previously and whose mass term corresponds to a Haldane term. We will see that the ideas we have shown already reappear as consequences of the full energy dispersion of the model.

The hamiltonian of the Chern insulator is:

$$H = \sin(k_x)\sigma_x + \sin(k_y)\sigma_y + B(2 + M - \cos(k_x) - \cos(k_y))\sigma_z \tag{2.57}$$

One of the low energy excitations corresponds to $k \approx 0$:

$$H \approx k_x\sigma_x + k_y\sigma_y + BM\sigma_z \tag{2.58}$$

which corresponds to bidimensional Dirac fermions with mass $m = BM$. This is not the only low energy excitation; for example at $(k_x, k_y) \approx (0, \pi)$,

$$H \approx k_x\sigma_x - k_y\sigma_y + B(2 + M)\sigma_z \tag{2.59}$$

This corresponds to another type of excitation of massive Dirac fermions. The relevance of the multiple gap closures lay down in that the Chern insulator has a more varied topological landscape than a simple massive Dirac fermion on the lattice; this happens because the Chern insulator is defined on a lattice and therefore has translational invariance. Thus, states that live on the edges of the Brillouin zone can also become low energy excitations.

Now let's examine the phase diagram of the Chern insulator in detail for the case of $B = 1$. The only values where the gap closes are at $M = 0$, $M = -2$ and $M = -4$. Due to our previous arguments, if we

adiabatically transform our hamiltonian from one value of M to another one without closing the gap, the topological nature of the system should not change.

1. $M > 0$ or $M < -4$ Phase

   These correspond to topologically trivial phases. Instead of doing calculations, we can see that $M > 0$ is equivalent to $M \to \infty$, and $M < -4$ is equivalent to $M \to -\infty$. Both of these cases correspond to the atomic limit, where if we think of the system as an electron tight-binding system, the hoppings are zero. This picture then means that the electrons are completely localized onsite in each atom of the insulator. If no conduction of electrons is possible, then σ_{xy} must be zero. But we have seen that the Hall conductivity is a topological invariant of a gapped band system, and since its zero, it must signal that the insulator is in a topologically trivial phase.

2. $-2 < M < 0$ Phase

   At $M = 0$ the gap closes at $(k_x, k_y) = (0, 0)$ as we have seen previously. The low energy excitations around this point are of the form of continuum 2D massive Dirac fermions with mass M and which have Hall conductivity $\sigma_{xy} = e^2 sgn(M)/2h$. In changing the phase from $M = 0^+$ to $M = 0^-$, we are changing the sign of M and therefore, the change of Hall conductivity must be $\Delta\sigma_{xy} = -e^2/h$. But since the previous phase had $\sigma_{xy}^{M>0} = 0$, we conclude that $\sigma_{xy}^{-2<M<0} = -e^2/h$. Then, since the Hall conductivity is a topological invariant, this phase is topologically non-trivial.

3. $-4 < M < -2$ Phase

   At $M = -2$ the gap closes at $(k_x, k_y) = (0, \pi)$ and $(k_x, k_y) = (\pi, 0)$. The low energy excitations around these points are of the form of continuum 2D massive Dirac fermions with mass $(2 + M)$ but with either the term with σ_x or σ_y with a changed sign. The Hall conductivity around these points is $\sigma_{xy} = -e^2 sgn(M + 2)/2h$[1]. In changing the phase from $M = -2^+$ to $M = -2^-$ we are changing the sign of $M + 2$ and therefore the change of Hall conductivity must be $\Delta\sigma_{xy} = -2e^2/h$. But since the previous phase had $\sigma_{xy}^{M>0} = -e^2/h$, we conclude that $\sigma_{xy}^{-4<M<2} = e^2/h$. Then, since the Hall conductivity is a topological invariant, this phase is a topologically non trivial phase. In addition, the Chern number associated with this phase is different from the $-2 < M < 0$ phase, therefore, even though both are topologically non trivial, they are of distinct characters.

A natural question that we can ask ourselves is, what is the difference between the two topological but distinct phases? The difference is in the sign of the Chern number, and therefore on the sign of the Hall conductivity associated at each phase. Electrons in an IQHE have quantized Landau orbits, and while the bulk ones complete their full cyclotron orbit, the electrons localized on the edge of the sample collide with the edges and hop around the boundaries of the system. The Chern number indicates the chirality of this cyclotron orbit, and thus the chirality of the edge state at the boundaries of the system. The difference in the two topological phases of the Chern insulator is then the chirality of the edge states [25].

Control over the different phases of topological insulators can lead to the development of novel quantum devices. In past years a plethora of different types of topological insulators have been discovered in the laboratory, opening the gateway for the development of these devices [38–48]. Even though we have only described the most basic of all topological insulators, the Chern Insulator, the underlying principles remain the same: the gapped electron bandstructure of a topological insulator has a topological invariant associated.

2.4 Graphene

To this point we have seen that topological insulators are playgrounds for the control of electronic excitations that behave as **massive** bidimensional Dirac fermions. A question that we can ask ourselves is: Are there any topological systems where the electronic excitations correspond to **massless** bidimensional Dirac fermions? The answer is Graphene.

[1] More generally, for a Hamiltonian of the form $H = k_\mu A_{\mu\nu}\sigma_\nu$, the Hall conductivity is given by $\sigma_{xy} = sgn(Det(A))/2$, In this case, the change of sign in one of the Pauli matrices changes the sign in the determinant of A.

Graphene was a longtime theorized material with outstanding properties that arise as a consequence of its topological nature. A record thermal conductivity and very high current density at room temperature, it is the strongest material known, it is highly flexible; the list goes on, and it seems that graphene is indeed a promising revolution in the field of materials science. Of high relevance was the synthetization of graphene in 2004 which resulted in the Nobel prize in physics for Konstantin Novoselov and Andre Geim [49]. Since then, graphene research has expanded to almost all STEM-related fields, and it's one of the most prolific research topics.

To understand graphene special properties, let's derive its electronic structure following closely [50]. Graphene consists of carbon atoms arranged in a bidimensional honeycomb structure. The valence orbitals of each atom hybridize to form three sp^2 bonds. Each atom has one conduction electron remaining in the corresponding nonbonding π orbital. The lattice can be regarded as a triangular bipartite Bravais lattice with two identical atoms per unit cell. Let's label the two atoms as A and B. The lattice basis vectors are:

$$\vec{a}_1 = a\Big(\frac{\sqrt{3}}{2}, \frac{1}{2}\Big) \quad \vec{a}_2 = a\Big(\frac{\sqrt{3}}{2}, -\frac{1}{2}\Big) \tag{2.60}$$

The reciprocal lattice vectors can be found using $\vec{a}_i \cdot \vec{b}_j = 2\pi\delta_{ij}$. The reciprocal lattice vectors are then

$$\vec{b}_1 = b\Big(\frac{1}{2}, \frac{\sqrt{3}}{2}\Big) \quad \vec{b}_2 = b\Big(\frac{1}{2}, -\frac{\sqrt{3}}{2}\Big) \tag{2.61}$$

with $b = 4\pi/a\sqrt{3}$. An illustration of both the Bravais lattice and the reciprocal lattice of graphene with the corresponding lattice vectors is shown in Figure 2.1.

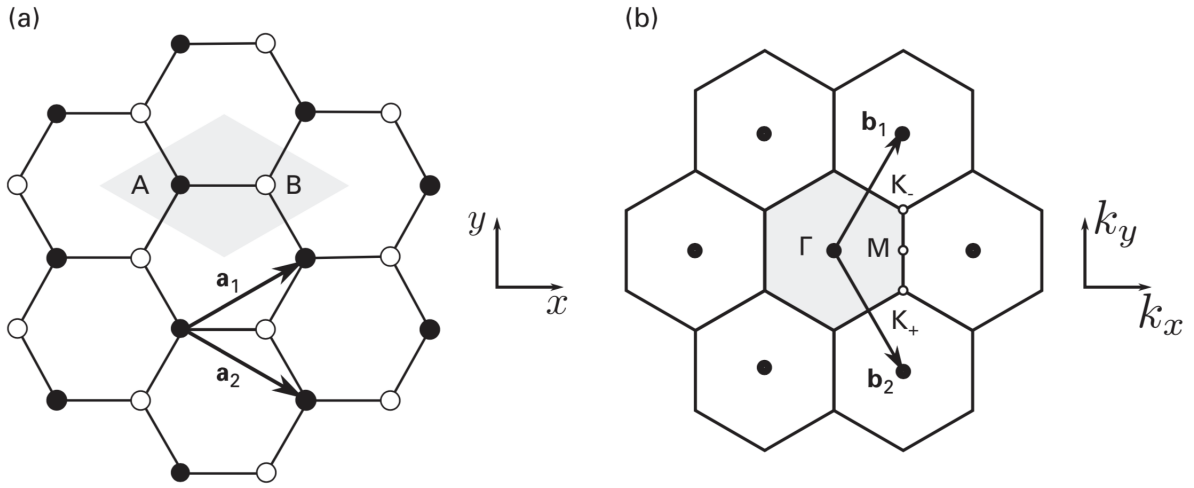

Figure 2.1: a) Schematical representation of the graphene Bravais lattice with the chosen lattice vectors $\vec{a}_1$ and $\vec{a}_2$ and the unit cell with the two A and B subsites. b) Schematical representation of the reciprocal lattice of graphene with the corresponding reciprocal lattice vectors $\vec{b}_1$ and $\vec{b}_2$. The Wigner-Seitz cell is shaded in gray in the figure, and the high symmetry points of the Brillouin zone are indicated. The figure is taken from [50], by courtesy of Luis Foa Torres.

Using Bloch theorem the Schrodinger equation for the electrons becomes:

$$\begin{pmatrix} \mathcal{H}_{AA}(\vec{k}) & \mathcal{H}_{AB}(\vec{k}) \\ \mathcal{H}_{BA}(\vec{k}) & \mathcal{H}_{BB}(\vec{k}) \end{pmatrix} \begin{pmatrix} c_A(\vec{k}) \\ c_B(\vec{k}) \end{pmatrix} = E(\vec{k}) \begin{pmatrix} c_A(\vec{k}) \\ c_B(\vec{k}) \end{pmatrix} \tag{2.62}$$

with

$$\begin{aligned}\mathcal{H}_{AA}(\vec{k}) &= \mathcal{H}_{BB}(\vec{k}) \\ &= \frac{1}{N_{cells}} \sum_{ij} e^{i\vec{k}\cdot(\vec{R}_j - \vec{R}_i)} \langle A_{\vec{R}_i} | \mathcal{H} | A_{\vec{R}_j} \rangle\end{aligned} \tag{2.63}$$

and

$$\begin{aligned}\mathcal{H}_{AB}(\vec{k}) &= \mathcal{H}^*_{BA}(\vec{k}) \\ &= \frac{1}{N_{cells}} \sum_{ij} e^{i\vec{k}\cdot(\vec{R}_j - \vec{R}_i)} \langle A_{\vec{R}_i} | \mathcal{H} | B_{\vec{R}_j} \rangle\end{aligned} \tag{2.64}$$

For graphene let the onsite energy be null, and the electron hopping only at first neighbors with a known transfer matrix $-\gamma_0$. Therefore:

$$\langle A_{\vec{R}_i} | \mathcal{H} | A_{\vec{R}_j} \rangle = 0 \tag{2.65}$$

$$\langle A_{\vec{R}_i} | \mathcal{H} | B_{\vec{R}_j} \rangle = -\gamma_0 \delta_{\vec{R}_i, \vec{R}_j + \vec{a}_\mu} \tag{2.66}$$

Here, $\vec{a}_\mu$ can be any of the primitive Bravais lattice vectors. Then, our Hamiltonian matrix elements become:

$$\mathcal{H}_{AA}(\vec{k}) = 0 \tag{2.67}$$

$$\begin{aligned}\mathcal{H}_{AB}(\vec{k}) &= -\gamma_0 (1 + e^{-i\vec{k}\cdot\vec{a}_1} + e^{-i\vec{k}\cdot\vec{a}_2}) \\ &= -\gamma_0 \alpha(\vec{k})\end{aligned} \tag{2.68}$$

where we have defined $\alpha(\vec{k}) = 1 + e^{-i\vec{k}\cdot\vec{a}_1} + e^{-i\vec{k}\cdot\vec{a}_2}$. With this, the Hamiltonian becomes:

$$\mathcal{H}(\vec{k}) = \begin{pmatrix} 0 & -\gamma_0 \alpha(\vec{k}) \\ -\gamma_0 \alpha(\vec{k})^* & 0 \end{pmatrix} \tag{2.69}$$

Therefore, the eigenenergies are:

$$E_\pm(\vec{k}) = \pm\gamma_0 |\alpha(\vec{k})| = \pm\gamma_0 \sqrt{3 + 2\cos(\vec{k}\cdot\vec{a}_1) + 2\cos(\vec{k}\cdot\vec{a}_2) + 2\cos(\vec{k}\cdot(\vec{a}_2 - \vec{a}_1))} \tag{2.70}$$

Plugging in the Bravais lattice vectors for graphene, we obtain:

$$E_\pm(k_x, k_y) = \pm\gamma_0 \sqrt{1 + 4\cos\left(\frac{\sqrt{3}k_x a}{2}\right)\cos\left(\frac{k_y a}{2}\right) + 4\cos^2\left(\frac{k_y a}{2}\right)} \tag{2.71}$$

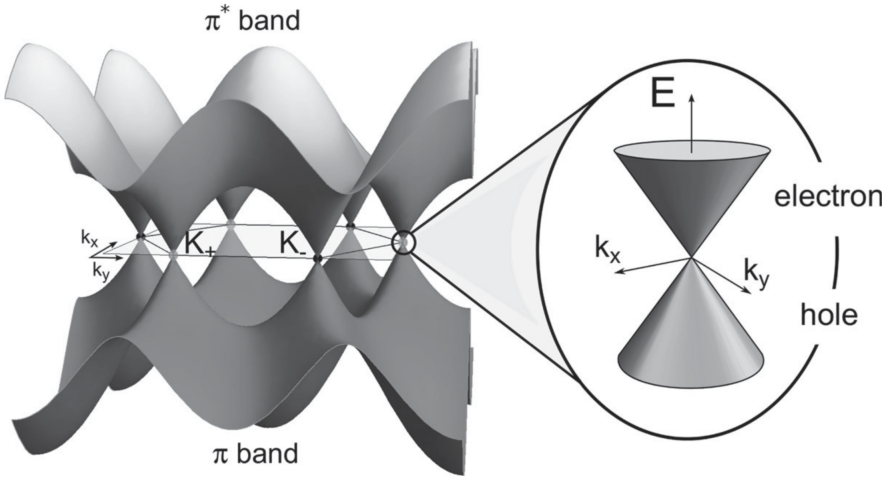

Figure 2.2: Schematical representation of graphene energy dispersion. Six Dirac cones, regions where the conduction and valence bands touch each other, are present in the first Brillouin zone at the inequivalent points $\vec{K}_+$ and $\vec{K}_-$. The figure is taken from [50], by courtesy of Luis Foa Torres.

The previous energy dispersion is shown in detail in Figure 2.2.

Let's investigate the low energy excitations of this bidimensional band dispersion. There are six corners in the Wigner-Seitz cell for the reciprocal space. Of these 6 points, only two of them are inequivalent, meaning that for one of the corners, we can get to 2 of the 5 remaining corners with reciprocal lattice vectors. Without loss of generality, let's choose the two inequivalent points as:

$$\vec{K}_+ = \frac{4\pi}{3a}\left(\frac{\sqrt{3}}{2}, -\frac{1}{2}\right) \quad \vec{K}_- = \frac{4\pi}{3a}\left(\frac{\sqrt{3}}{2}, \frac{1}{2}\right) \tag{2.72}$$

where we can check that $\alpha(\vec{K}_+) = \alpha(\vec{K}_-) = 0$, and thus $E(\vec{K}_+) = E(\vec{K}_-) = 0$. These are the only points in the reciprocal space where the energy becomes null. Therefore, we can conclude that the bandstructure is entirely gapped save for six points in the Brillouin zone, of which only two of them are inequivalent between each other. The touching of the valence and conduction bands at these points can be seen in detail in Figure 2.2.

How do the low energy excitations behave around these crossing points? Let $\vec{k} = \vec{K}_+ + \delta\vec{k}$. Then,

$$\begin{aligned} \alpha(\vec{k}) &\simeq \nabla_{\vec{k}}\alpha(\vec{K}_+)\delta\vec{k} \\ &= \frac{\sqrt{3}a}{2}\delta\vec{k} \end{aligned} \tag{2.73}$$

Then,

$$E_\pm \simeq \pm\frac{\sqrt{3}a\gamma_0}{2}|\delta\vec{k}| = \pm v_F|\delta\vec{k}| \tag{2.74}$$

where we have defined $v_F = \sqrt{3}\gamma_0 a/2$ as the Fermi velocity. These low energy excitations correspond to the energy dispersion of massless bidimensional Dirac fermions. Expanding the energy around the $\vec{K}_-$ point gives out the same result.

Moreover, expanding the Hamiltonian around these points, we get

$$\begin{aligned}\mathcal{H}_{\vec{K}_+} &\simeq v_F \begin{pmatrix} 0 & k_x - ik_y \\ k_x + ik_y & 0 \end{pmatrix} \\ &= v_F(k_x\sigma_x + k_y\sigma_y)\end{aligned} \tag{2.75}$$

with $\mathcal{H}_{\vec{K}_-} = \mathcal{H}^\dagger_{\vec{K}_+}$. Recalling 2.47 we see that the Hamiltonian around these points is equivalent to that of massless bidimensional Dirac fermions. From now on, we will call these band energy crossings *Dirac cones*.

It's important to note that here the Pauli matrices correspond to pseudo-spin, related to the existence of two bipartite sublattices in the graphene lattice, and are not the proper spin of the electron.

We can resume the information on both inequivalent cones defining $e^{i\theta_k} = (k_x + ik_y)/k$. Let ξ be a variable that takes the value $\xi = +1$ when expanding around $\vec{K}_+$ and $\xi = -1$ when expanding around $\vec{K}_-$. Then, we can write the low energy expansion as:

$$\mathcal{H}_\xi(\vec{k}) = v_F|\vec{k}| \begin{pmatrix} 0 & e^{-i\xi\theta_k} \\ e^{+i\xi\theta_k} & 0 \end{pmatrix} \tag{2.76}$$

The eigenvectors of this Hamiltonian are readily avalaible and are:

$$|\psi_{\xi,s}\rangle = \frac{1}{\sqrt{2}} \begin{pmatrix} 1 \\ se^{+i\xi\theta_k} \end{pmatrix} \tag{2.77}$$

where the index s indicates either the conduction band ($s = +1$) or the valence band ($s = -1$).

We've seen that the low energy excitations are of massless Dirac fermions. Let's answer now why are they topological. We have previously stated that a band theory must be gapped to have a well defined Chern number. Since the spectrum of graphene is gapless, we can't compute a Berry curvature associated with the system. Nonetheless, the Berry connection doesn't get undefined with a gapless system, and we can compute the Berry phase as:

$$\gamma_C = \int_C \vec{A} \cdot d\vec{k} \tag{2.78}$$

In particular, let's compute the Berry phase for a system whose adiabatic evolution (in $\vec{k}$) circles around the $\vec{K}_+$ cone. The Berry connection is:

$$\begin{aligned}\vec{A} &= -i\langle\psi_{1,s}|\nabla_k|\psi_{1,s}\rangle \\ &= -\frac{i}{2}\begin{pmatrix} 1 & se^{-i\theta_k} \end{pmatrix} \cdot \begin{pmatrix} 0 \\ i(\nabla_k\theta_k)se^{i\theta_k} \end{pmatrix} \\ &= -\frac{is^2\hat{\theta}}{2k}\begin{pmatrix} 1 & e^{-i\theta_k} \end{pmatrix} \cdot \begin{pmatrix} 0 \\ ie^{i\theta_k} \end{pmatrix} \\ &= \frac{\hat{\theta}}{2k}\end{aligned} \tag{2.79}$$

Therefore, the Berry phase associated with this evolution is:

$$\begin{aligned}\gamma_C &= \int_C \vec{A} \cdot d\vec{k} \\ &= \int_0^{2\pi} \frac{\hat{\theta}}{2k} \cdot k d\theta \hat{\theta} \\ &= \pi\end{aligned} \tag{2.80}$$

For the $\vec{K}_-$ cone, the associated Berry phase is $-\pi$. Both results are consistent with a topologically non-trivial system. Therefore graphene is a topologically non-trivial material provided that the evolution of the Hamiltonian in the parameter space $\vec{k}$ encircles either an even number of $\vec{K}_+$ Dirac cones and an odd number of $\vec{K}_-$ Dirac cones, or vice-versa.

Let's examine in detail one of the most direct consequences of the topology of graphene. Let's define the helicity operator as:

$$\hat{h} = \hat{\sigma} \cdot \hat{k} \tag{2.81}$$

The eigenvalues of this operator are $h = \pm 1$, which correspond to right-handed and left-handed chirality correspondingly. For the low-energy Hamiltonian, since we are dealing with only two Pauli matrices, $[\mathcal{H}, \hat{h}] = 0$. Therefore, the eigenstates of the low-energy Hamiltonian have well-defined chirality, and in particular, the two inequivalent Dirac cones have opposite chiralities. Therefore, the chirality, which is equivalent to if either the components to the electron pseudospin are parallel or antiparallel (provided the value of s is fixed) is locked to the momentum of the electron. The chirality of the electron in each cone and band is shown schematically in Figure 2.3.

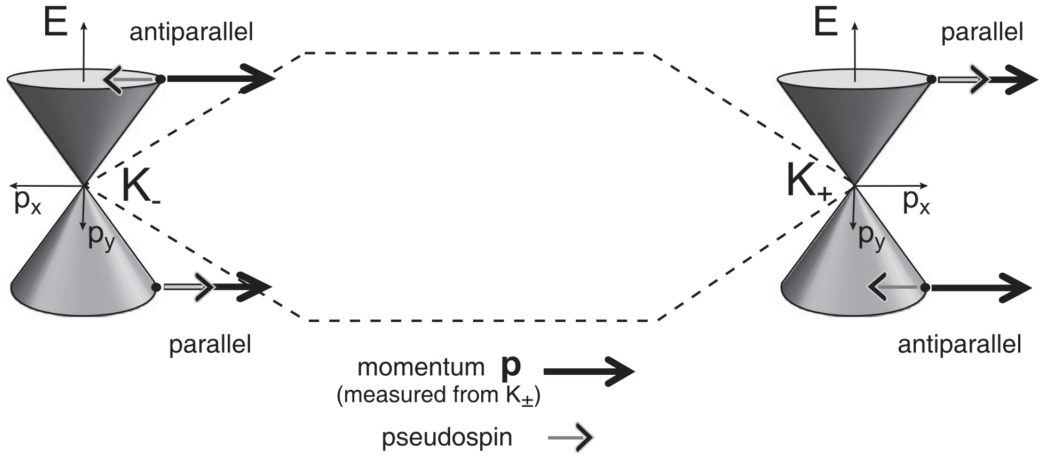

Figure 2.3: Schematical representation of the reversal of pseudospin and chirality when interchanging the electron between the two inequivalent Dirac cones $\vec{K}_-$ and $\vec{K}_+$. The figure is taken from [50], by courtesy of Luis Foa Torres.

The previous statement is equivalent to establishing that graphene has an absence of backscattering. Suppose we have a conduction electron with a definite momentum $\vec{k}$. If the electron scatters elastically with an impurity of the material, it's momentum has to reverse to $-\vec{k}$. But in reversing the momentum, we are also changing the chirality of the electron. The change of chirality is prohibited since the eigenstates of the electron have definite chirality. Therefore, backscattering is impossible in graphene unless we add a perturbation that reverses the pseudospin of the electron [51]. This argumentation helps to begin explaining the myriad of extreme properties that graphene has in contrast with non-topological materials that we established at the beginning of this section.

Chapter 3

Weyl Semimetals

We now have the theoretical background to understand topological band theory. With this, we can answer the first of the questions we proposed at the beginning of this thesis: What are Weyl semimetals?

3.1 General Aspects

At the end of the previous chapter, we established that graphene is a bi-dimensional material where the low energy excitations correspond to massless bidimensional Dirac fermions. We can ask ourselves a new question: is there a system where the low energy excitations correspond to Weyl fermions? The answer is that such systems exist and are called Weyl semimetals.

Weyl semimetals are materials that are realized exclusively in three dimensions instead of two dimensions. Unlike graphene, where the electronic dispersion hosts doubly-degenerate Dirac nodes, Weyl semimetals host pairs of non-degenerate Weyl nodes with definite and opposing chiralities. In addition, Weyl semimetals are topologically protected by the dimensionality of the material instead of symmetries as in graphene.

The Weyl nodes are discrete points in $\vec{k}$ space where the conduction and valence energy bands meet linearly, forming a Weyl cone. The low energy excitations around these points correspond to Weyl fermions quasiparticles that satisfy the Weyl equation [2]:

$$i\hbar\sigma^{\mu}\partial_{\mu}\psi = 0 \tag{3.1}$$

The Weyl equation comes from considering a massless version of the Dirac equation 2.47, where the Gamma matrices and the four-component fermion spinor, by consequence of having a null mass, decouples in two identical equations as 3.1. Here, all three Pauli matrices are present ($\mu = \{x, y, z\}$), and the solution corresponds to massless fermions with two-component spinors representing a spin 1/2 particle of a definite chirality χ. We can represent the previous Hamiltonian $\mathcal{H}_{\chi}$ as [3]:

$$\mathcal{H}_{\chi} = \chi v_F k_{\mu}\sigma^{\mu} \tag{3.2}$$

and the Energy dispersion near the Weyl cones as:

$$E_{\pm}(\vec{k}) = \pm v_F|\vec{k}| \tag{3.3}$$

An schematical representation of this energy dispersion is shown in Figure 3.1. Let us rewrite the Hamiltonian in equation 3.3 as:

$$\mathcal{H} = f_0(\vec{k})\mathbb{I} + f_1(\vec{k})\sigma_x + f_2(\vec{k})\sigma_y + f_3(\vec{k})\sigma_z \tag{3.4}$$

To establish a band crossing in the band-structure of this Hamiltonian, we need to fine-tune three independent parameters in the Hamiltonian to be zero, i.e., $f_1 = f_2 = f_3 = 0$, which in turn can only happen on a three-dimensional space. Therefore, this proves that Weyl semimetals must always be tridimensional materials.

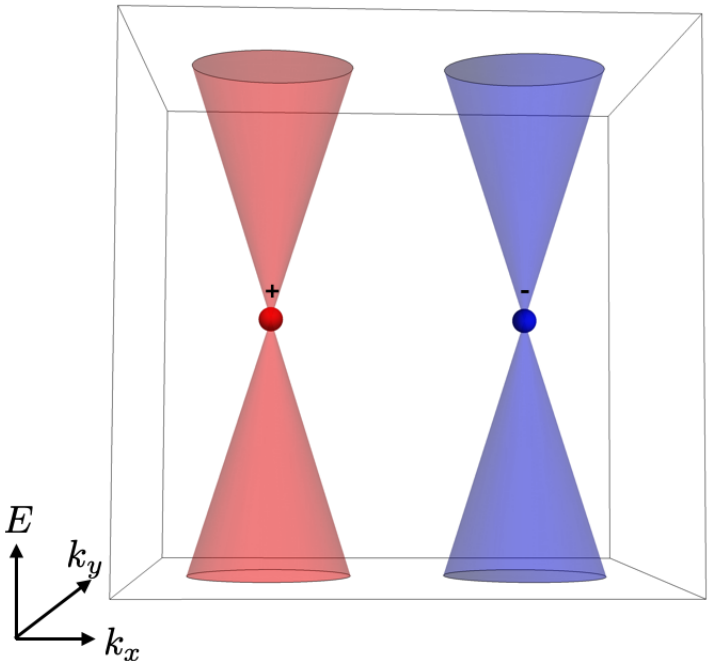

Figure 3.1: Schematical representation of the Energy dispersion for a pair of Weyl nodes in the reciprocal space. The chirality of the nodes is labeled, and for a pair they must satisfy that the net chirality is zero.

As each Weyl node has a definite chirality, the particles that arise from the Weyl equation also have a definite chirality. Due to the Nielsen-Nynomiya theorem, also called the fermion doubling theorem, a non-interacting lattice-hopping model such as the one that Weyl semimetals present cannot have a net imbalance of chirality provided a weak number of restrictions apply [52, 53]. Then, Weyl nodes must always come in pairs, so that no chiral fermion remains unpaired, and the net chirality remains balanced. Each node in the pair will have a definite chirality, where one of the Weyl nodes will act as a source of Berry flux, and the other one will serve as a drain of Berry flux [54].

Note that adding a perturbation, for example, with a term containing σ_z, will only shift the Weyl nodes in $\vec{k}$ space and not open a gap between the bands [3]. Consequently, we establish that Weyl nodes are topologically protected by the dimensionality. This is in contrast to graphene, where a perturbation of the form $m\sigma_z$ adds a mass term to the Dirac fermions and thus opens the gap, deleting its topological properties.

Multilayer stacking of topological insulators have been proposed and studied as building blocks for constructing tridimensional Weyl semimetals with just one pair of Weyl nodes [16, 55]. Therefore, we can think of each bidimensional layer that does not contain a Weyl node, as a gapped topological insulator that can be on a trivial or a non-trivial topological phase. In addition, since we know that there are topologically protected edge states in topological insulators, we can expect by construction that a Weyl semimetal in a topological phase will have topologically protected surface states.

The structure of a Weyl semimetal is gapless, thus, defining a Chern number or another topological invariant with the eigenfunctions in the entire $\vec{k}$ space is impossible. But, as we did in graphene, we can come around this problem. In particular, we can use the chirality of Weyl nodes as a means in understanding the topological phases of the semimetal.

Suppose we have a pair of Weyl nodes that emit Berry flux with the field lines passing through the inside of the nodes, as shown in Figure 3.2 a. The plane situated in the insider, which is a Chern insulator, will have Berry flux passing through it and, therefore, will be in a topological phase. If we calculate the Chern number associated with that plane, we will find that it takes a non-zero integer value. In contrast, if we take a plane situated outside the nodes, no Berry flux will pass through the plane, and the topological insulator will be in a trivial topological phase, with no associated Chern number. If the Weyl pair had the field lines passing through the inside of the nodes, we would have the reversed situation of Figure 3.2 b. The takeaway is that one of the two planes will always carry a non-null topological invariant for a pair of topological Weyl nodes.

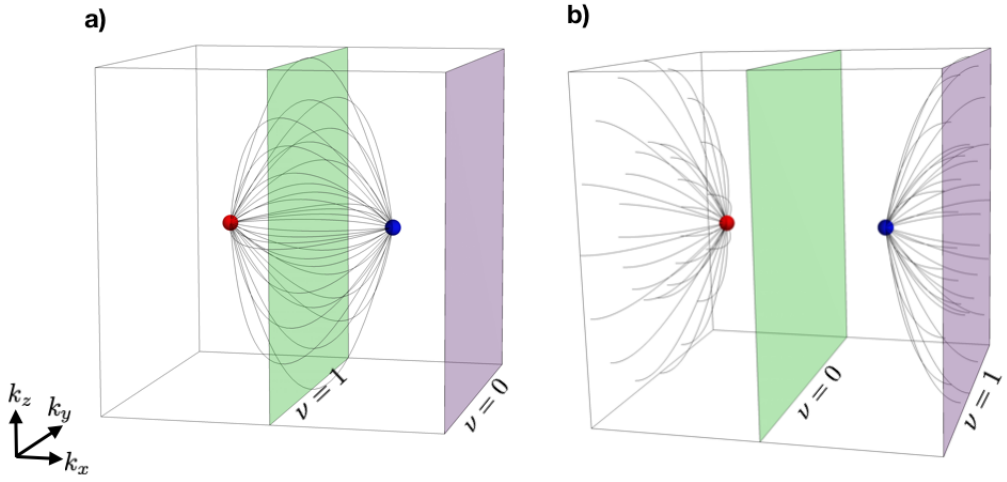

Figure 3.2: Schematical representation of a Weyl nodes pair with Chern insulator planes situated inside and outside the nodes and the Berry flux field lines are drawn. In a), we have a situation where the Berry field lines close through the inside of the nodes; therefore, the planes in between the nodes has a non-null Chern number while the planes outside the nodes have a null Chern number. In b) the Berry field lines close through the outside of the nodes; therefore the situation is reversed; the plane inside has non-null Chern number and the plane outside null Chern number.

In conclusion, the tools for examining the topological landscape of Weyl semimetals will be using Chern insulators layers that are situated in between and outside all pairs of Weyl nodes in the bulk band-structure. For a semimetal with more than one pair of nodes, the topological landscape can become incredibly complex and rich, and a high number of bidimensional planes must be used to understand the different phases [2].

Let's examine some of the characteristic properties of Weyl semimetals in a more detailed way in the following sections.

3.2 Breaking of Symmetries

In the previous section, we established that Weyl cones are non-degenerate. We will now see that to have non-degenerate Weyl nodes we must impose that our Weyl semimetals break either Time-Reversal Symmetry (TRS) or Inversion Symmetry (IS).

Consider a system with half-integer spin particles preserving simultaneously TRS and IS, and with a low energy Hamiltonian satisfying 3.3. The accidental crossings in momentum space can either be degenerate (Dirac points) or non-degenerate (Weyl points). Kramers theorem implies that for a Hamiltonian that preserves Parity symmetry, the band spectrum $E(\vec{k})$ must be at least doubly degenerate [1]. Therefore, if

[1]For a spectrum $E(\vec{k})$ of a Hamiltonian $\mathcal{H}$ that has translational invariance, Kramers theorem requires parity symmetry instead of time-reversal symmetry for the energy bands to be doubly-degenerate [24].

an accidental crossing is present on the band structure, it will be degenerate and correspond to a Dirac point [2].

Since Parity symmetry is composed of the combination of TRS and IS, one of the two must be broken for the degeneracy of the Dirac point to be lifted and to separate the two degenerate copies of the Dirac cones in a pair of Weyl cones with different chiralities and positions in reciprocal space. [2]

We already know due to the Fermion Doubling theorem that the minimum number of Weyl nodes in a semimetal is 2, each one with complementary chiralities. For TRS breaking Weyl semimetals this remains as the minimum number [55], but for IS breaking semimetals, the minimum number of Weyl nodes is 4 because, since TRS is preserved, a node of chirality χ at a point $\vec{k}_0$ in Brillouin space has to have a symmetric partner of the same chirality at $-\vec{k}_0$; since the total chirality must be zero, there must be a minimum of 4 nodes in these types of semimetals [54].

3.3 Fermi Arcs

The Fermi surfaces of Weyl semimetals are one of the most essential and key signatures of these materials since they carry associated unique topological properties and are the gateway to observing Weyl semimetals in the laboratory. They correspond to the intersection of Surface bands, a projection of the bulk band-structure due to finite size geometry, and the Fermi energy [55].

As shown from Figure 3.3a, for just one pair of nodes, the surface band will be a projection of both Weyl cones onto a tangent surface to the cones. Therefore, the intersection with the Fermi energy corresponds to an open line that goes from one Weyl cone projection to the opposite projection.

The Fermi surface by itself remains open, which contradicts what is known for Fermi surfaces. The answer to this is that there can be two surfaces to use as the intersection with the Fermi surface. Combining the Fermi arcs from both surfaces, we can construct ourselves a closed Fermi surface that passes through the cones projections, as shown in Figure 3.3b [56].

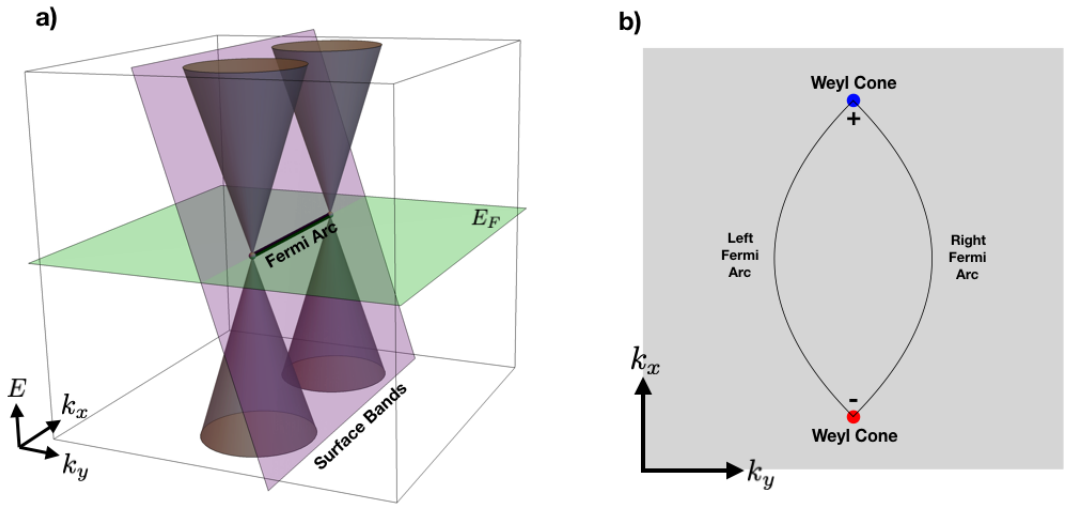

Figure 3.3: a) Schematical representation of a Fermi arc, the Fermi surface created by the intersection between the Fermi energy, and the surface bands of a pair of Weyl nodes. b) Schematical representation of the projection of the Weyl nodes onto the surface band; the Fermi arcs become a closed Fermi surface by the combination of the states from both surfaces.

3.4 Anomalous Quantum Hall Effect

Let's derive the Landau levels for a single Weyl cone of chirality χ. Let's take the Hamiltonian of equation 3.2 and introduce the minimal coupling to an external magnetic field.

$$\mathcal{H} = \chi v_F(\vec{k} - q\vec{A}) \cdot \vec{\sigma} \tag{3.5}$$

We take without loss of generality the magnetic field in the z direction $\vec{B} = B\hat{z}$ and the vector potential in the symmetric gauge $\vec{A} = (-By/2, Bx/2, 0)$. Introducing transformed momentum operators,

$$\Pi_x = k_x + \frac{qBy}{2} \quad \Pi_y = k_y - \frac{qBx}{2} \tag{3.6}$$

that satisfy $[\Pi_x, \Pi, y] = iqB$, and ladder operators

$$a = \sqrt{\frac{1}{2qB}}(\Pi_x + i\Pi_y) \quad a^\dagger = \sqrt{\frac{1}{2qB}}(\Pi_x - i\Pi_y) \tag{3.7}$$

that satisfy $[a, a^\dagger] = 1$. We can rewrite the hamiltonian as:

$$\begin{aligned} \mathcal{H} &= \chi v_F[(k_x - qA_x)\sigma_x + (k_y - qA_y)\sigma_y + k_z\sigma_z] \\ &= \chi v_F[\Pi_x\sigma_x + \Pi_y\sigma_y + k_z\sigma_z] \\ &= \chi v_F\sqrt{2qB}(a\sigma_- + a^\dagger\sigma_+) + \chi v_F k_z\sigma_z \end{aligned} \tag{3.8}$$

Three quantum numbers then characterize our states, the Landau level n, the spin of the electron $\uparrow, \downarrow$, and the momentum in the direction parallel to the magnetic field k_z. The ground state of this Hamiltonian, corresponding to the zeroth Landau level, has special properties. The energy is:

$$\begin{aligned} E_0|0, \uparrow, k_z\rangle &= \mathcal{H}|0, \uparrow, k_z\rangle \\ &= \chi v_F k_z|0, \uparrow, k_z\rangle \end{aligned} \tag{3.9}$$

because $a|0, \uparrow, k_z\rangle = 0$ and $\sigma_+|0, \uparrow, k_z\rangle = 0$. We can't use the $|0, \downarrow, k_z\rangle$ state for the zero'th Landau level since it is not an eigenstate of the Hamiltonian.

The rest of the landau levels are found by squaring the Hamiltonian. Using that $\chi^2 = 1$:

$$\begin{aligned} \mathcal{H}^2 &= 2v_F^2 qB(a\sigma_- + a^\dagger\sigma_+)^2 + v_F^2 k_z^2\sigma_z^2 + v_F^2 k_z\sqrt{2qB}(a\{\sigma_-, \sigma_z\} + a^\dagger\{\sigma_+, \sigma_z\}) \\ &= 2v_F^2 qB(aa^\dagger\sigma_-\sigma_+ + a^\dagger a\sigma_+\sigma_-) + v_F^2 k_z^2 \\ &= 2v_F^2 qB(a^\dagger a\{\sigma_+, \sigma_-\} + \sigma_-\sigma_+) + v_F^2 k_z^2 \\ &= qBv_F^2(2a^\dagger a + 1 - \sigma_z) + v_F^2 k_z^2 \end{aligned} \tag{3.10}$$

Where we have used numerous properties of the Pauli matrices and the ladder operators. Using this, the landau levels satisfy:

$$\begin{aligned} E_{n,\uparrow}^2|n, \uparrow, k_z\rangle &= \mathcal{H}^2|n, \uparrow, k_z\rangle \\ &= (2qBv_F^2 n + v_F^2 k_z^2)|n, \uparrow, k_z\rangle \end{aligned} \tag{3.11}$$

$$
\begin{aligned}
E^2_{n,\downarrow}|n,\uparrow,k_z\rangle &= \mathcal{H}^2|n,\downarrow,k_z\rangle \\
&= (2qBv_F^2(n+1)+v_F^2k_z^2)|n,\downarrow,k_z\rangle
\end{aligned}
\tag{3.12}
$$

so that $E_{n,\uparrow} = \pm v_F\sqrt{2qBn+k_z^2}$ and $E_{n,\downarrow} = \pm v_F\sqrt{2qB(n+1)+k_z^2}$.

A few peculiarities arise from these Landau levels. The zeroth Landau level is the only one that is chiral dependent, and that disperses in only one direction (notice the omission of the $\pm$ sign). For the remaining levels, there is a peculiarity in that the Weyl cones Landau levels also disperse in the direction of the magnetic field. This is in contrast to massive electrons, where the levels are magnetic field independent, and to graphene, where the offset to n is absent, and the $n = 0$ Landau level is magnetic field independent [57, 58].

For TRS breaking Weyl semimetals, the combination of the two Landau levels from the cones are filled up with the intrinsic Berry field generated by the nodes (instead of an external magnetic field). Therefore, a giant Anomalous Quantum Hall Effect (AQHE) arises that is proportional to the momentum separation of the Weyl cones [16, 59–61].

$$
\sigma_{yz} = \frac{e^2}{2\pi h}(k_+ - k_-) \tag{3.13}
$$

For IS breaking Weyl semimetals, the AQHE disappears because the two copies of Weyl nodes with the same chirality cancel each other's Berry phase. Nevertheless, a Quantum Spin Hall Effect is still present for these types of systems [62].

3.5 Chiral Anomaly

The Chiral Anomaly is the condensed matter analog of the Adler-Bell-Jackiw anomaly in high energy physics. For massless fermions in odd spatial dimensions, a Chiral Symmetry appears [63, 64]. In a vacuum system, the total chiral charge must be conserved to preserve the symmetry; therefore, an unpaired Weyl fermion with a chirality χ cannot appear on a $3+1$ universe. But for a condensed matter system, such as a Weyl semimetal, we can come around this problem and break the Chiral symmetry.

For one Weyl node, the continuity equation for electrons with Chiral symmetry is modified as:

$$
\dot{n} + \vec{\nabla}\cdot\vec{J} = \chi\frac{e^2}{4\pi^2h^2c}\vec{E}\cdot\vec{B} \tag{3.14}
$$

Therefore, taking into account the pair of Weyl nodes, the difference of densities between the two cones is:

$$
\begin{aligned}
\frac{d\Delta n}{dt} &= \dot{n}_+ - \dot{n}_- \\
&= \frac{e^2}{2\pi^2h^2c}\vec{E}\cdot\vec{B}
\end{aligned}
\tag{3.15}
$$

Consequently, charge can be pumped from one cone of one chirality to another by applying simultaneously parallel electric and magnetic fields to a Weyl semimetal. Then, the Chiral anomaly arises because the fields break chiral symmetry, and the net chirality becomes non-null. Consequences of the Chiral anomaly in Weyl semimetals are the appearance of a negative Magneto-Resistance and special non-local transport and optical properties [5, 58, 65–67].

3.6 Experimental Realizations

As we have previously stated, Fermi arcs are the key signature of Weyl semimetals because they are a unique and peculiar type of Fermi surface that is not present in other topological materials. With the usage of ARPES (Angle-Resolved Photoemission Spectroscopy), one can distinguish the presence of Fermi arcs in crystal structures experimentally. Using high-energy ARPES, one can obtain the dispersion associated with the bulk Weyl cones while using low-energy ARPES, one can obtain the surface dispersion and the Fermi arcs. The bridge between the theoretical prediction of Weyl semimetals was short-lived, and in the year 2005, the first discovery of a real Weyl semimetal was published [9]. In Figure 3.4, the ARPES images from that discovery are presented, and we can see precisely the Fermi arcs for this material.

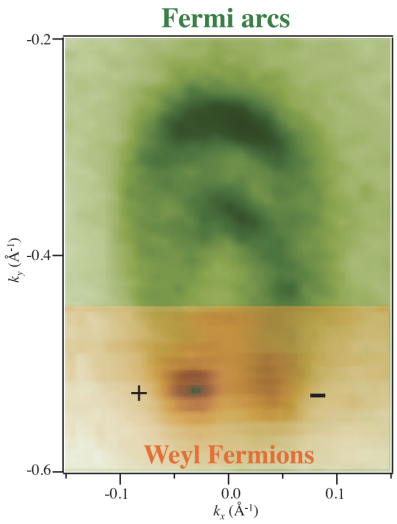

Figure 3.4: Low-energy ARPES image of a TaAs family Weyl semimetal (green), superimposed over a High-energy ARPES image of the same material. The Weyl cones, and the associated Fermi arc can be easily appreciated. Figure from [9]. Reprinted with permission from AAAS.

Shortly after, a discovery wave of IS breaking type of Weyl semimetals began with numerous findings such as the tantalum arsenide (TaAs) family semimetals [9, 11, 68, 69], the niobium arsenide (NbAs) semimetal [70], and the tantalum phosphide (TaP) semimetal [71] to name a few ones; The TRS breaking type of Weyl semimetals had escaped direct detection until this present year with the discovery of [13].

Chapter 4

Quantum Transport

Provided the theoretical background for understanding what are Weyl semimetals, we now turn to the second question we asked ourselves: *What do we mean when we talk about transport, more specifically, quantum transport?* The concepts we will examine in this chapter are more general than topological systems: quantum transport applies to all condensed matter materials where electrons can propagate, not necessarily freely, throughout the system. Understanding quantum transport allows us to connect experimental results with topological signatures of materials.

4.1 Landauer-Büttiker Formalism

Let's picture a device connected to a number of electrodes with an applied voltage bias. How does the electron propagation look inside the device? What is the current flowing through the device? In principle, answering these types of questions involves solving the Schrodinger equation for all electrons, something that is inadequate since numerous scattering processes, either with the material or between them, can occur for each one of the electrons. A framework for approximating the system must be chosen.

When choosing a framework, we must ask ourselves, is the regime of propagation *sequential* or *coherent*? Suppose the electrodes have some associated energy levels that couple to the device and in which the electron that enters the material has a defined lifetime τ_D before exiting the device. As the electron propagates, scattering processes take place, and the wavefunction starts to lose coherence. Therefore, for each system, we can associate a decoherence time τ_ϕ in which the number of scattering processes makes the electron wavefunction lose complete coherence. If $\tau_\phi \gg \tau_D$ we are in a coherent regime, otherwise, for $\tau_\phi \ll \tau_D$ we are in a sequential regime.

Sequential regimes are well suited for a semiclassical picture of electron transport, where the electrons are injected in the device, loses complete coherence and become "classical," before exiting the device. For a coherent regime, the quantum nature of the electron takes the leading role, and a framework that takes into account both the electrodes and the device interactions must be built.

The Landauer-Büttiker formalism is a framework for coherent transport that provides us with a way of calculating currents flowing through a device, in the function of the transmission coefficients of an electron propagating through the system. Since topological signatures on materials rely heavily on the quantum nature of the electrons, this coherent regime is well suited for the simulations carried on the following chapter. Let us now derive the Landauer-Buttiker formula.

Consider the most simple picture of a transport experiment. A device (D) connected to two leads, the left lead (L) and the right lead (R) as shown in Figure 4.1. Both leads act as reservoirs of electrons with chemical potentials μ_L and μ_R. Provided that the chemical potentials are different, turning on the coupling between leads and the system takes the system out of equilibrium; the steady-state equilibrium is achieved when a steady current I flows through the device. Landauer-Buttiker formula attempts to bridge the value

of the current I with the chemical potentials μ_L and μ_R.

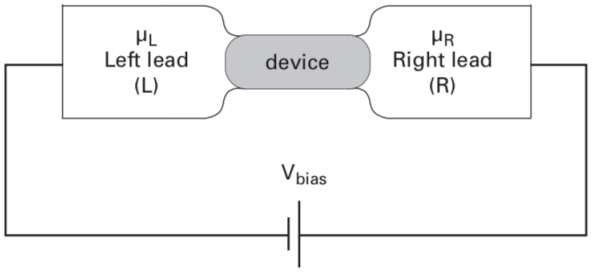

Figure 4.1: Schematical representation of a device (D) connected to a left lead (L) and a right lead (R) subjected to a bias voltage. The figure is taken from [50], by courtesy of Luis Foa Torres.

The following derivation follows closely the one in [72]. Let the electrons in the leads be represented by fermionic operators $\{c^\dagger_{k\alpha}, c_{k\alpha}\}$, with k the momentum and $\alpha = \{L, R\}$ and index representing the left or right lead; and the electrons in the device be represented with fermionic operators $\{d^\dagger_n(t), d_n(t)\}$ with n a band index. The Hamiltonian of the entire system is:

$$H = \sum_{k\alpha} \epsilon_{k\alpha} c^\dagger_{k\alpha} c_{k\alpha} + H_{device}(\{d^\dagger_n(t)\}; \{d_n(t)\}) + \sum_{k\alpha n} (\gamma_{k\alpha,n} c^\dagger_{k\alpha} d_n(t) + h.c.) \tag{4.1}$$

Where we have divided the hamiltonian in the hamiltonian of the leads, the hamiltonian of the device, and the device/lead interaction controlled by a coupling γ. The current flowing from the device to the left lead can be written as a balance equation between a quantum of current multiplied by all the modes that the electrons can be created in the left lead and get destroyed in the device, minus the quantum of current multiplied by all the modes in which the electrons can get destroyed in the left lead and created in the device, and everything multiplied by 2 accounting for the electron spin degeneracy:

$$I_{D\to L} = \frac{2ie}{\hbar} \int \frac{d\omega}{2\pi} \sum_{kn} (\gamma_{kL,n} \langle c^\dagger_{kL} d_n \rangle - \gamma^*_{kL,n} \langle d^\dagger_n c_{kL} \rangle) \tag{4.2}$$

We introduce the Keldysh many-body Green's functions as [73]:

$$G^<_{n,k\alpha}(t) = i\langle c^\dagger_{k\alpha} d_n(t) \rangle \quad G^<_{k\alpha,n}(t) = i\langle d_n(t) c^\dagger_{k\alpha} \rangle \quad G^<_{n,m}(t) = i\langle d^\dagger_n d_m(t) \rangle \tag{4.3}$$

$$G^>_{n,k\alpha}(t) = -i\langle d_n(t) c^\dagger_{k\alpha} \rangle \quad G^>_{k\alpha,n}(t) = -i\langle c_{k\alpha} d_n(t)^\dagger \rangle \quad G^>_{n,m}(t) = -i\langle d_m(t) d^\dagger_n \rangle \tag{4.4}$$

$$G^t = \Theta(t<0) G^>(t) + \Theta(t>0) G^<(t) \tag{4.5}$$

$$G^{\tilde{t}} = \Theta(t>0) G^>(t) + \Theta(t<0) G^<(t) \tag{4.6}$$

as the Lesser Green's function, the Greater Green's function, the Time-Ordered Green's function, and the Antitime-Ordered Green's function respectively. Therefore, we can rewrite the current as:

$$I_{D\to L} = \frac{2e}{\hbar} \int \frac{d\omega}{2\pi} \sum_{kn} (\gamma_{kL,n} G^<_{n,kL}(\omega) - \gamma^*_{kL,n} G^<_{kL,n}(\omega)) \tag{4.7}$$

In the Keldysh formalism, we can write the Dyson equation for the perturbed Green's functions in matricial form [73]:

$$\hat{G}^{(1)}(1,1') = \hat{G}^{(0)}(1,2)\hat{V}(2)\hat{G}^{(0)}(2,1') \tag{4.8}$$

where

$$\hat{G} = \begin{pmatrix} G^t & G^< \\ G^> & G^{\tilde{t}} \end{pmatrix} \quad \hat{V} = \begin{pmatrix} V(2) & 0 \\ 0 & -V(2) \end{pmatrix} \tag{4.9}$$

$\hat{G^{(1)}}$ is the interacting Green's function for the complete system, $\hat{G^{(0)}}$ is the unperturbed Green's function, and $V(2)$ is the interaction part of the Hamiltonian. For this system in particular, we have:

$$\hat{G}^{(1)}_{k\alpha,n} = \sum_m \hat{G}^{(0)}_{k\alpha,k\alpha}\hat{V}_{k\alpha,m}\hat{G}^{(0)}_{m,n} \tag{4.10}$$

We will drop the superscripts, and differentiate the unperturbed Green's functions of the lead with a minuscule $\hat{g}$. Then:

$$\hat{G}_{k\alpha,n} = \sum_m \hat{g}_{k\alpha,k\alpha}\hat{V}_{k\alpha,m}\hat{G}_{m,n} \tag{4.11}$$

Writing explicitly the matrices we have:

$$\begin{aligned} \begin{pmatrix} G^t_{k\alpha,n} & G^<_{k\alpha,n} \\ G^>_{k\alpha,n} & G^{\tilde{t}}_{k\alpha,n} \end{pmatrix} &= \sum_m \begin{pmatrix} g^t_{k\alpha,k\alpha} & g^<_{k\alpha,k\alpha} \\ g^>_{k\alpha,k\alpha} & g^{\tilde{t}}_{k\alpha,k\alpha} \end{pmatrix} \begin{pmatrix} \gamma_{k\alpha,m} & 0 \\ 0 & -\gamma_{k\alpha,m} \end{pmatrix} \begin{pmatrix} G^t_{m,n} & G^<_{m,n} \\ G^>_{m,n} & G^{\tilde{t}}_{m,n} \end{pmatrix} \\ &= \sum_m \gamma_{k\alpha,m} \begin{pmatrix} g^t_{k\alpha,k\alpha} & g^<_{k\alpha,k\alpha} \\ g^>_{k\alpha,k\alpha} & g^{\tilde{t}}_{k\alpha,k\alpha} \end{pmatrix} \begin{pmatrix} G^t_{m,n} & G^<_{m,n} \\ -G^>_{m,n} & -G^{\tilde{t}}_{m,n} \end{pmatrix} \end{aligned} \tag{4.12}$$

Therefore:

$$G^<_{kL,n}(\omega) = \sum_m \gamma_{kL,m}[g^t_{kL,kL}(\omega)G^<_{m,n}(\omega) - g^<_{kL,kL}(\omega)G^{\tilde{t}}_{m,n}(\omega)] \tag{4.13}$$

By analogy for the other perturbed Green function of interest we have:

$$G^<_{n,kL}(\omega) = \sum_m \gamma^*_{kL,m}[g^<_{kL,kL}(\omega)G^t_{n,m}(\omega) - g^{\tilde{t}}_{kL,kL}(\omega)G^<_{n,m}(\omega)] \tag{4.14}$$

Using the previous equations in 4.7:

$$
\begin{aligned}
I_{D\to L} &= \frac{2e}{\hbar}\int\frac{d\omega}{2\pi}\sum_{knm}(\gamma_{kL,n}\gamma^*_{kL,m}[g^<_{kL,kL}(\omega)G^t_{n,m}(\omega)-g^{\tilde{t}}_{kL,kL}(\omega)G^<_{n,m}(\omega)] \\
&\qquad -\gamma^*_{kL,n}\gamma_{kL,m}[g^t_{kL,kL}(\omega)G^<_{m,n}(\omega)-g^<_{kL,kL}(\omega)G^{\tilde{t}}_{m,n}(\omega)]) \\
&= \frac{2e}{\hbar}\int\frac{d\omega}{2\pi}\sum_{knm}\gamma_{kL,n}\gamma^*_{kL,m}[g^<_{kL,kL}(\omega)G^t_{n,m}(\omega)-g^{\tilde{t}}_{kL,kL}(\omega)G^<_{n,m}(\omega)-g^t_{kL,kL}(\omega)G^<_{n,m}(\omega) \\
&\qquad +g^<_{kL,kL}(\omega)G^{\tilde{t}}_{n,m}(\omega)] \\
&= \frac{2e}{\hbar}\int\frac{d\omega}{2\pi}\sum_{knm}\gamma_{kL,n}\gamma^*_{kL,m}[g^<_{kL,kL}(\omega)(G^t_{n,m}(\omega)+G^{\tilde{t}}_{n,m}(\omega))-(g^t_{kL,kL}(\omega)+g^{\tilde{t}}_{kL,kL}(\omega))G^<_{n,m}(\omega)]
\end{aligned}
\tag{4.15}
$$

From equations 4.5 and 4.6 we see directly that $G^t + G^{\tilde{t}} = G^< + G^>$. Therefore:

$$
\begin{aligned}
I_{D\to L} &= \frac{2e}{\hbar}\int\frac{d\omega}{2\pi}\sum_{knm}\gamma_{kL,n}\gamma^*_{kL,m}[g^<_{kL,kL}(\omega)(G^<_{n,m}(\omega)+G^>_{n,m}(\omega))-(g^<_{kL,kL}(\omega)+g^>_{kL,kL}(\omega))G^<_{n,m}(\omega)] \\
&= \frac{2e}{\hbar}\int\frac{d\omega}{2\pi}\sum_{knm}\gamma_{kL,n}\gamma^*_{kL,m}[g^<_{kL,kL}(\omega)G^>_{n,m}(\omega)-g^>_{kL,kL}(\omega)G^<_{n,m}(\omega)]
\end{aligned}
\tag{4.16}
$$

The unperturbed Green's functions in the lead ($g(\omega)$) correspond to a free electron gas, which functions are known [73]:

$$
g^<_{kL,kL}(\omega) = 2\pi i f_L(\omega)\delta(\omega-\epsilon_{kL}+\mu_L) \tag{4.17}
$$

$$
g^>_{kL,kL}(\omega) = -2\pi i(1-f_L(\omega))\delta(\omega-\epsilon_{kL}+\mu_L) \tag{4.18}
$$

Using equations 4.17 and 4.18 we have:

$$
\begin{aligned}
I_{D\to L} &= \frac{2ie}{\hbar}\int d\omega\sum_{knm}\gamma_{kL,n}\gamma^*_{kL,m}[f_L(\omega)G^>_{n,m}(\omega)-(1-f_L(\omega))G^<_{n,m}(\omega)]\delta(\omega-\epsilon_{kL}+\mu_L) \\
&= \frac{2ie}{\hbar}\sum_{knm}\gamma_{kL,n}\gamma^*_{kL,m}[f_L(\epsilon_{kL}-\mu_L)G^>_{n,m}(\epsilon_{kL})-(1-f_L(\epsilon_{kL}-\mu_L))G^<_{n,m}(\epsilon_{kL})] \\
&= \frac{2ie}{\hbar}\sum_{knm}\gamma_{kL,n}\gamma^*_{kL,m}[f_L(\epsilon_{kL}-\mu_L)(G^>_{n,m}(\epsilon_{kL})-G^<_{n,m}(\epsilon_{kL}))+G^<_{n,m}(\epsilon_{kL})]
\end{aligned}
\tag{4.19}
$$

The subtraction of the lesser and greater Green's functions can be written in the function of the retarded and advanced Green's functions [73]:

$$
G^> - G^< = G^r - G^a \tag{4.20}
$$

Then:

$$
\begin{aligned}
I_{D\to L} &= \frac{2ie}{\hbar}\sum_{knm}\gamma_{kL,n}\gamma^*_{kL,m}[f_L(\epsilon_{kL}-\mu_L)(G^r_{n,m}(\epsilon_{kL})-G^a_{n,m}(\epsilon_{kL}))+G^<_{n,m}(\epsilon_{kL})] \\
&= \frac{2ie}{\hbar}\sum_{nm}\int d\epsilon D_L(\epsilon)\gamma_n(\epsilon)\gamma^*_m(\epsilon)[f_L(\epsilon-\mu_L)(G^r_{n,m}(\epsilon)-G^a_{n,m}(\epsilon))+G^<_{n,m}(\epsilon)]
\end{aligned}
\tag{4.21}
$$

where we have introduced the density of states $D_L(\epsilon)$. Let's introduce the Broadening functions as $\Gamma^L_{m,n}(\epsilon) = 2\pi D_L(\epsilon)\gamma_n(\epsilon)\gamma^*_m(\epsilon)$ that account for the non-hermicity of the interaction part of the Hamiltonian. Using this:

$$I_{D\to L} = \frac{2ie}{h}\sum_{nm}\int \Gamma^L_{m,n}(\epsilon)[f_L(\epsilon-\mu_L)(G^r_{n,m}(\epsilon) - G^a_{n,m}(\epsilon)) + G^<_{n,m}(\epsilon)]d\epsilon \tag{4.22}$$

Repeating the same lengthy procedure, we can also conclude for the right lead:

$$I_{D\to R} = \frac{2ie}{h}\sum_{nm}\int \Gamma^R_{m,n}(\epsilon)[f_R(\epsilon-\mu_R)(G^r_{n,m}(\epsilon) - G^a_{n,m}(\epsilon)) + G^<_{n,m}(\epsilon)]d\epsilon \tag{4.23}$$

In the Landauer-Buttiker we are searching for the steady-state solution to the current, that is $I_{D\to L} = I_{R\to D} = I$. Symmetrizing:

$$\begin{aligned} I &= \frac{1}{2}(I_{D\to L} + I_{R\to D}) \\ &= \frac{1}{2}(I_{D\to L} - I_{D\to R}) \\ &= \frac{ie}{h}\sum_{nm}\int [(f_L(\epsilon-\mu_L)\Gamma^L_{m,n}(\epsilon) - f_R(\epsilon-\mu_R)\Gamma^R_{m,n}(\epsilon))(G^r_{n,m}(\epsilon) - G^a_{n,m}(\epsilon)) + (\Gamma^L_{m,n}(\epsilon) - \Gamma^R_{m,n}(\epsilon))G^<_{n,m}(\epsilon)]d\epsilon \end{aligned} \tag{4.24}$$

In matrix notation, the sum of indexes can be written as a trace of matrix functions:

$$I = \frac{ie}{h}\int Tr[(f_L(\epsilon-\mu_L)\Gamma^L - f_R(\epsilon-\mu_R)\Gamma^R)(G^r - G^a) + (\Gamma^L - \Gamma^R)G^<]d\epsilon \tag{4.25}$$

We can use additional identities regarding the Keldysh Green's functions [73]:

$$G^< = if_L G^r\Gamma^L G^a + if_R G^r\Gamma^R G^a \tag{4.26}$$

$$G^r - G^a = -iG^r(\Gamma^L + \Gamma^R)G^a \tag{4.27}$$

Using these equations we arrive at:

$$I = \frac{ie}{h}\int Tr[(-i(f_L\Gamma^L - f_R\Gamma^R)G^r(\Gamma^L + \Gamma^R)G^a + i(\Gamma^L - \Gamma^R)(f_L G^r\Gamma^L G^a + if_R G^r\Gamma^R G^a)]d\epsilon \tag{4.28}$$

With some algebraic manipulations, we conclude that:

$$I = \frac{2e}{h}\int d\epsilon[f_L(\epsilon-\mu_L) - f_R(\epsilon-\mu_R)]Tr[G^a\Gamma^R G^r\Gamma^L] \tag{4.29}$$

In virtue of the trace formula [72], $Tr[G^a\Gamma^R G^r\Gamma^L]$ is equal to the total transmission coefficient $T(\epsilon)$ between the left and right leads:

$$I = \frac{2e}{h}\int d\epsilon[f_L(\epsilon-\mu_L) - f_R(\epsilon-\mu_R)]T(\epsilon) \tag{4.30}$$

Equation 4.30 is the Landauer-Buttiker Formula and is a powerful tool to calculate currents in a device with just the information of the total transmission coefficient, which in turn can be easily calculated by numerical tools. An useful generalization of the Landauer formula is to multiple leads connected to one device. In this setup the current I_j passing through an electrode j is: [50]

$$I_j = \frac{2e}{h}\sum_i \int d\epsilon[T_{j,i}(\epsilon)f_i(\epsilon-\mu_i) - T_{i,j}(\epsilon)f_j(\epsilon-\mu_j)] \tag{4.31}$$

The last formula will be useful to calculate non-local conductances in a device, which we will detail in the following section.

4.2 Multiterminal Conductance

As we have stated in Chapter 2, topological materials are often signaled by the appearance of a quantized Hall conductance due to edge states propagating in the device. In addition, a null longitudinal conductance appears in these materials. We want to use Landauer-Buttiker formula to show how in an experiment for topological materials, these results appear. The bulk of the explanation carried here follows [74].

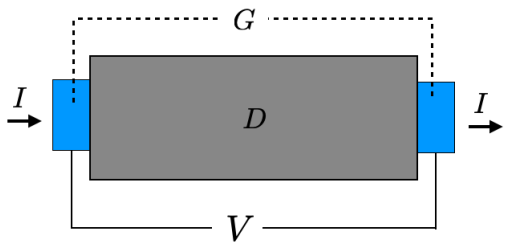

Figure 4.2: Schematical representation of a two-terminal conductance measurement.

Traditionally, we define Hall conductances and longitudinal conductances in virtue of the Hall effect. Picture a device connected to two leads with a current applied through the two terminals, as shown in Figure 4.2; the total two-terminal conductance can be computed in virtue of Ohm's law:

$$I = GV \tag{4.32}$$

In any Hall effect phenomena, we expect electron motions to deviate from the lead to lead trajectory and thus, to charge to accumulate on the edges of the sample. If we, therefore, introduce two extra leads that attach themselves perpendicular to the applied current path, we will measure a voltage difference between the probes, even though no current has been applied between these two extra probes. Therefore, our transport experiment has a picture, as shown in Figure 4.3. To account for these two types of conductances that we can measure, we promote in Ohm's law the conductance to a matrix and the current and voltage to vectors:

$$\begin{pmatrix} I_x \\ I_y \end{pmatrix} = \begin{pmatrix} G_{xx} & G_{xy} \\ G_{yx} & G_{yy} \end{pmatrix} \begin{pmatrix} V_x \\ V_y \end{pmatrix} \tag{4.33}$$

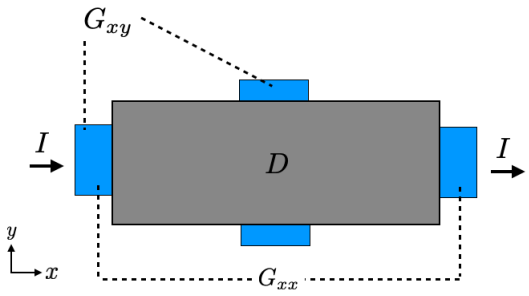

Figure 4.3: Schematical representation of a four-terminal Hall experiment, with the measurements of longitudinal conductances G_{xx} and Hall conductances G_{xy}.

In this scheme, the longitudinal conductances correspond to the diagonal responses to transport (G_{xx} and G_{yy}) while the Hall conductances correspond to the off-diagonal responses to transport (G_{xy} and G_{yx}).

It would seem that a minimum of 4 leads is then needed to obtain both the diagonal and off-diagonal responses in a Hall effect transport experiment. But there is a problem; the connection of the leads with materials is often invasive and modifies the conductances properties than can be measured in-within the probe. This is a manifestation of the measurement of local transport properties. To measure non-local transport properties (i.e., that do not depend on the properties of the leads and only of the bulk properties of the device), we need an additional two leads so that measurements of the transport properties can be done between leads where no current is applied.

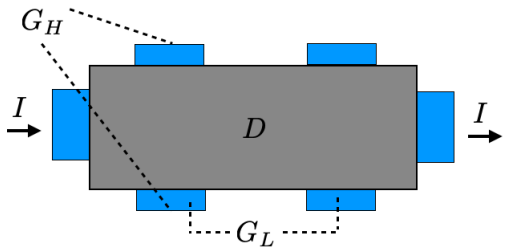

Figure 4.4: Schematical representation of a six-terminal Hall experiment, with the measurements of non-local longitudinal conductances G_L and non-local Hall conductances G_H.

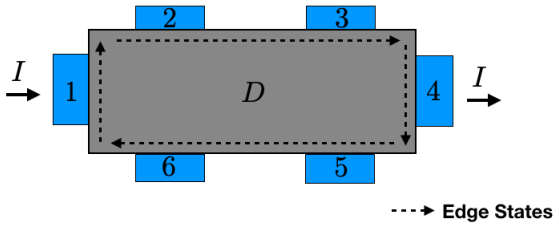

Figure 4.5: Schematical representation of a six-terminal Hall experiment with leads numbered 1 to 6, and the edge states propagating through the device for a system in a Quantum Hall Effect.

Consider a six-terminal Hall bar experiment as shown on Figure 4.4. Let's suppose that a number M of edge states propagate in one direction through the edges of the device as shown on Figure 4.5. The transmission coefficients between all leads can be summarized as:

$$T_{pq} = \begin{cases} M & \text{if } (p,q) = \{(1,6),(2,1),(3,2),(43),(5,4),(6,5)\} \\ 0 & \text{otherwise} \end{cases} \tag{4.34}$$

The conductance matrix elements are related to the transmission matrix elements as:

$$G_{pq} = \frac{2e^2}{h} T_{pq} \tag{4.35}$$

Then:

$$\begin{aligned} G_{pq} &= \begin{cases} \frac{2e^2 M}{h} & \text{if } (p,q) = \{(1,6),(2,1),(3,2),(4,3),(5,4),(6,5)\} \\ 0 & \text{otherwise} \end{cases} \\ &= \begin{cases} G & \text{if } (p,q) = \{(1,6),(2,1),(3,2),(4,3),(5,4),(6,5)\} \\ 0 & \text{otherwise} \end{cases} \end{aligned} \tag{4.36}$$

Meanwhile, if in each probe there is a voltage V_j, the occupations satisfy $f_j = eV_j$. Therefore, we can rewrite Landauer-Buttiker equation 4.31 as:

$$I_p = \sum_q [G_{qp} V_p - G_{pq} V_q] \tag{4.37}$$

The conductances satisfy a sum rule:

$$\sum_q G_{qp} = \sum_q G_{pq} \tag{4.38}$$

Then, we can further rewrite the Landauer equation as:

$$I_p = \sum_q G_{pq} [V_p - V_q] \tag{4.39}$$

Using 4.36 and 4.39:

$$\begin{pmatrix} I_1 \\ I_2 \\ I_3 \\ I_4 \\ I_5 \\ I_6 \end{pmatrix} = \begin{pmatrix} G & 0 & 0 & 0 & 0 & -G \\ -G & G & 0 & 0 & 0 & 0 \\ 0 & -G & G & 0 & 0 & 0 \\ 0 & 0 & -G & G & 0 & 0 \\ 0 & 0 & 0 & -G & G & 0 \\ 0 & 0 & 0 & 0 & -G & G \end{pmatrix} \begin{pmatrix} V_1 \\ V_2 \\ V_3 \\ V_4 \\ V_5 \\ V_6 \end{pmatrix} \tag{4.40}$$

Since voltages differences are the important value to measure, we can set without loss of generality one of the lead probes voltage to 0. Let's choose $V_4 = 0$. Then, $I_4 = -GV_3$, and we can reduce the system of equations to:

$$\begin{pmatrix} I_1 \\ I_2 \\ I_3 \\ I_5 \\ I_6 \end{pmatrix} = \begin{pmatrix} G & 0 & 0 & 0 & -G \\ -G & G & 0 & 0 & 0 \\ 0 & -G & G & 0 & 0 \\ 0 & 0 & 0 & G & 0 \\ 0 & 0 & 0 & -G & G \end{pmatrix} \begin{pmatrix} V_1 \\ V_2 \\ V_3 \\ V_5 \\ V_6 \end{pmatrix} \tag{4.41}$$

Let's set the current flowing between terminal 1 and 4. Then, $I_1 = -I_4 = I$ and $I_2 = I_3 = I_5 = I_6 = 0$. We have the equations:

$$I = G(V_1 - V_6) \quad V_1 = V_2 = V_3 \quad V_5 = V_6 = 0 \tag{4.42}$$

Therefore, applying the Ohm's law we can calculate the longitudinal conductance, using the probes number 2 and 3, and the Hall conductance using the probes number 2 and 6, all of them which have no current flowing through them.

$$\begin{aligned} R_H &= \frac{V_2 - V_3}{I} \\ &= 0/I \\ &= 0 \end{aligned} \tag{4.43}$$

$$\begin{aligned} G_L &= \frac{I}{V_2 - V_6} \\ &= \frac{I}{V_1 - V_6} \\ &= \frac{I}{I/G} \\ &= G \\ &= 2M \ \frac{e^2}{h} \end{aligned} \tag{4.44}$$

So therefore, we can conclude that for a topological system with quantized propagating edge states, the longitudinal resistance vanishes and the Hall conductance gets quantized in $2M$ units of e^2/h which signals the appearance of a QHE. In the research carried in this thesis, we will use the connection between Landauer-Buttiker's formula and Ohm's law to calculate non-local transport properties in a Weyl semimetal.

Chapter 5

Multi-terminal Conductance at the Surface of a Weyl Semimetal

We have now presented the tools needed to understand the general aspects of what makes Weyl semimetals different to other topological systems, and of electron coherent quantum transport. As we have stated on chapter 3, Weyl semimetals present unique surface states that are connected to the Fermi arcs that appear on the band structure of a finite sample of the semimetal. Despite the intense research on the transport properties of these materials, an understanding of the topological role in the transport properties of the surfaces has been missing.

In this chapter we propose a simple "hydrogen-like" model of a Weyl semimetal that breaks Time Reversal Symmetry and study a topological phase in which only one pair of nodes is present. By using a multi-terminal Hall experiment on the surface of this semimetal, we will elucidate what topological properties are unique to the Fermi arcs. The results here have been published in [75].

5.1 Hamiltonian Model

For our calculations we use a model of spinful electrons on a cubic lattice (one orbital per site with lattice constant a) [2, 16],

$$\begin{aligned}\mathcal{H}_k = &[2t_x\left(\cos(k_x)-\cos(k_0)\right)+\\ &+m\left(2-\cos(k_y)-\cos(k_z)\right)]\sigma_x+\\ &+2t_y\sin(k_y)\sigma_y+2t_z\sin(k_z)\sigma_z.\end{aligned} \tag{5.1}$$

As noticed in Ref. [16], this model has two, four, six or eight Weyl nodes depending on the interplay between the hoppings t_x, t_y, t_z and the mass term determined by m. Each pair of nodes is related by *inversion symmetry* which is preserved as there is a single orbital per site and only one site in the lattice basis.

The breaking of the *time reversal symmetry* is governed by the parameter m in the Hamiltonian. Let us analyze this in more detail. The time-reversal operator $\mathcal{T}$ can be written as $\mathcal{T}=\mathcal{U}\theta$, where $\mathcal{U}$ is a unitary operator and θ is the complex conjugation operator ($\theta^{-1}=\theta$ (see for example [76], chapter 2), one can also show that $\theta\sigma_x\theta=\sigma_x$, $\theta\sigma_y\theta=-\sigma_y$ and $\theta\sigma_z\theta=\sigma_z$). For spin 1/2 particles, the unitary operator must have the form: $\mathcal{U}=e^{i\phi}\sigma_y$, with ϕ an arbitrary phase. This satisfies all the required conditions for a time-reversal operator: it is anti-unitary, changes the sign of spin and is a 2×2 matrix. The second condition can be expressed as: $\mathcal{T}\sigma_j\mathcal{T}^\dagger=-\sigma_j$.

5.2 Electronic Structure

For the electronic structure and transport calculations that follow we set $t_x = t_y = t_z = 1/2$. This leaves the parameter m free to control the topological phases of the semimetal. We use two 2D Brillouin planes perpendicular to k_x to characterize the phases; one situated at $k_x = 0$ and one situated at $k_x = \pi$. This ensures that the first plane is always in between all the nodes present in the reciprocal space, while the second one being at the edge of the first Brillouin zone, will always be outside of all the nodes.

We calculate the Chern number on both planes as function of m, as shown on Fig. 5.1. We find five topological phases, which can be grouped in three groups of distinct topological phases.

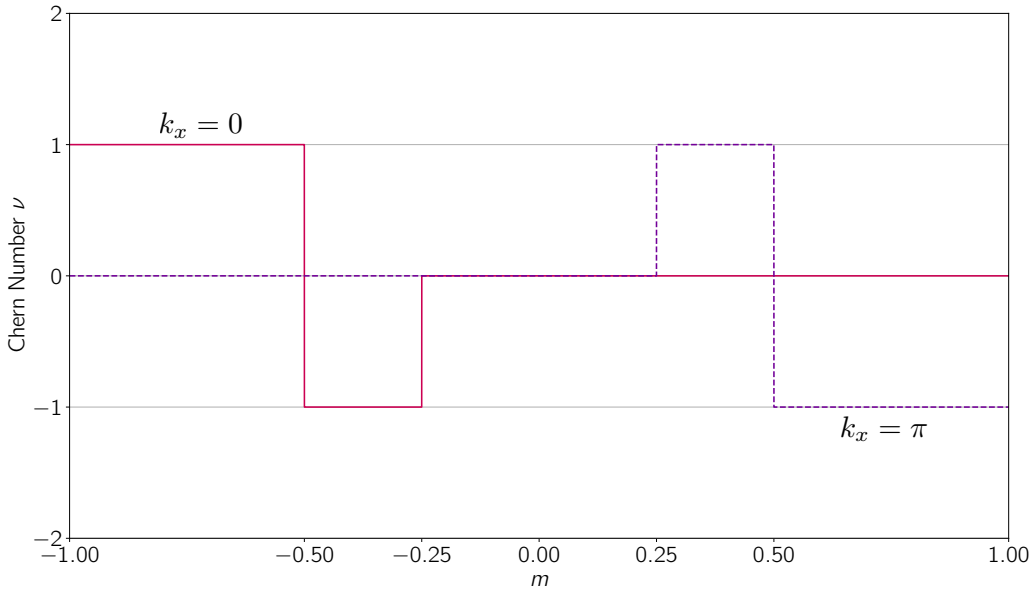

Figure 5.1: Values of the Chern number ν for the planes intersecting $k_x = 0$ and $k_x = \pi/a$ in the Brillouin zone, as a function of m.

The first group corresponds to $|m| < 0.25$ and it presents 4 pair of Weyl nodes on the electronic structure. The second ground corresponds to $0.25 < |m| < 0.5$ and it presents 3 pair of Weyl nodes on the dispersion. Finally, the last group corresponds to $|m| > 0.5$ and it only presents one pair of Weyl nodes. The two phases that compose the second and third group differ on the location of the Berry field lines; for one phase they close through the inside of the Brillouin zone (therefore $\nu_{k_x=0} \neq 0$), and for the other one they close through the outside of the Brillouin zone ($\nu_{k_x=0} \neq \pi$). Despite the difference on the topological invariants for the pair of phases, the only change between the two in the group is in the chirality of the surface states.

As we have stated before, we'd like to elucidate the topological properties of only one pair of Weyl nodes so therefore, we choose $m = 1.0$ so that our model contains only two Weyl nodes located at $\vec{k} = (\pm\pi/2a, 0, 0)$ as shown in the bulk dispersion calculated along high symmetry points in Fig. 5.2(a). This phase is characterized by a Chern number $\nu = 0$ in the 2D Brillouin planes located between the Weyl nodes, and a Chern number $\nu = -1$ in the planes located outside of the nodes (see Fig. 5.2(b)). The topological nature of this phase motivates us to ask about the transport response originated by the surface states in this minimal case, but before turning to this question, we need to review its electronic structure in more detail.

The numerical calculations were implemented in Python using the modules: Kwant [77] and Python tight-binding[1].

As mentioned earlier, the Fermi arcs are gapless bands that connect the projections of the Weyl nodes in a given plane of the Brillouin zone. Since we are in a phase with a single pair of nodes, only one Fermi

[1]The Python Tight-Binding package is available at this link

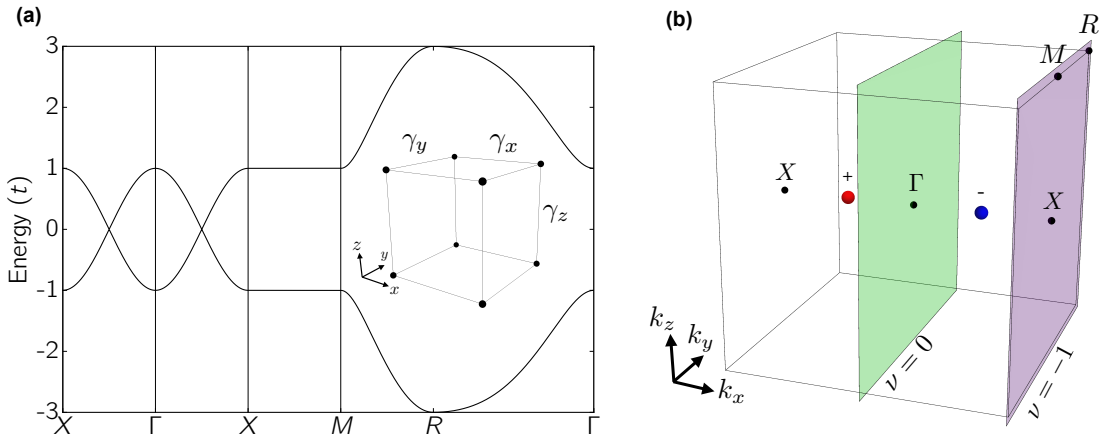

Figure 5.2: (a) Bulk dispersion of the semimetal in the topological phase with only two Weyl nodes with parameters $m = 1.0$, and $t_x = t_y = t_z = 1/2$. The inset shows a cell of the real space lattice with nearest neighbor hoppings γ_x, γ_y, γ_z. (b) First Brillouin zone of the Weyl semimetal showing the high symmetry points where the dispersion in (a) was calculated. We show also the Weyl nodes of opposite chirality, and the planes where the Chern numbers were obtained.

arc is to be expected on this surface. To evidence the Fermi arcs we need to terminate the system at the correct surface. Figure 5.3(a) and (b) show the band structure for a system with 100 lattice sites in the z-direction (and infinite on the other two). In Fig. 5.3(a), the two gapless bands at zero energy form the Fermi arc. Nevertheless, these dispersionless bands associated to the Fermi arc in the k_x direction do have a non-vanishing group velocity along k_y as shown in Fig. 5.3(b).

Next, we focus on the electronic structure of a Weyl semimetal wire with a square cross-section of 30×30 lattice sites in the xy, xz and yz planes respectively. The band structures for the wires are shown in Fig. 5.3(c) and (d). Figure 5.3(c) corresponds to a wire extending along z (i.e. with the cross-section in the xy plane), the results for a wire extending along y are identical. The projection of the two Weyl Nodes is a single Dirac cone that is doubly degenerate and hosts edge states around its center. The wire with the cross-section in the yz plane has a different band structure as shown in Fig. 5.3(d). Flat bands appear around $E_F = 0$ that do not carry associated edge states. These flat bands are the manifestation of the Fermi arcs: due to the to finite size effects of the wire geometry they present a splitting which scales with $1/N^2$.

5.3 Multiterminal Transport Response

Let us now turn to the transport response of this 'hydrogen-model' of a Weyl semimetal. We are interested, in particular, in a Hall setup at one of the surfaces of a three-dimensional sample. Specifically, we consider six two-dimensional electrodes connected (in an H-configuration) to the surface of a rectangular cuboid as represented in Fig. 5.4(g). Note that this differs from other works where the sample is accessed with the electrodes on the full volume [78, 79] and not just the surface. In the following we present simulations for a rectangular cuboid of $180 \times 30 \times 30$ lattice sites in the x, y and z-directions, respectively. Each lead is described by a two-dimensional square lattice with lattice constant matching that of the 3D cuboid and 30 lattice sites in width. The separation between the voltage probes is set to 120 lattice sites. The 2D lattice has nearest neighbors and spin independent hoppings equal to $t_{lead} = 1.0$. This value also characterizes the hopping from sites in the leads to the matching points in our structure.

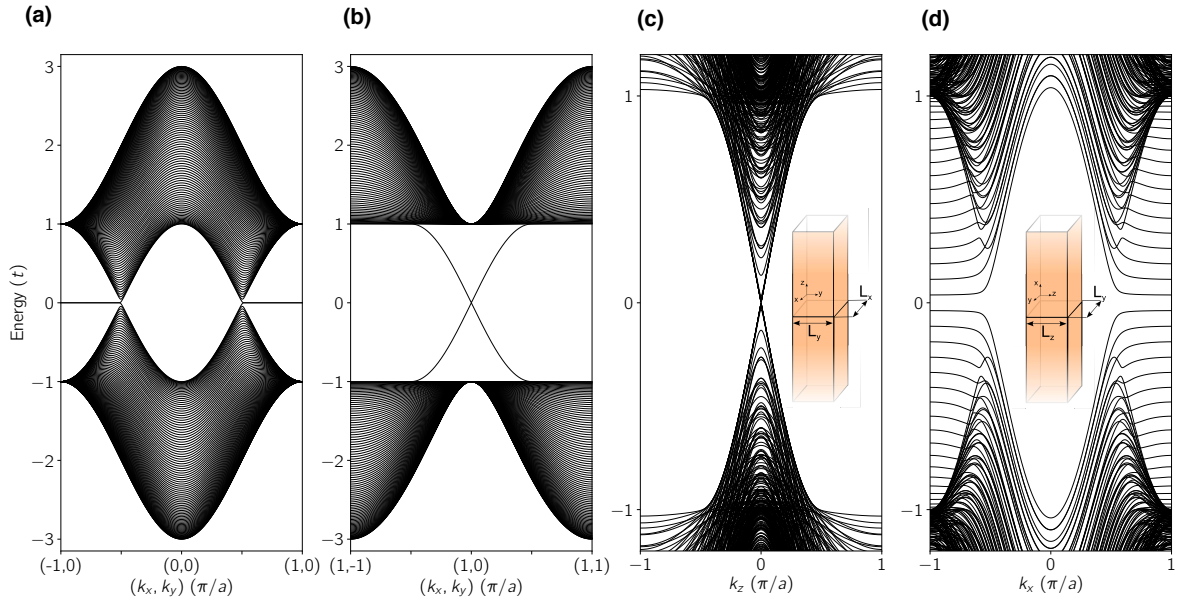

Figure 5.3: Energy dispersions for the model discussed in the text. (a) and (b) correspond to a system with 100 lattice sites in the z-direction (and infinite in x and y). (a) shows the dispersion along the $k_y = 0$ line in the 2D Brillouin zone, while (b) shows it along the $k_x = \pi/a$ line. (c) and (d) show the energy dispersion for a Weyl semimetal wire with a cross section of 30×30 lattice sites (with the same parameters as in (a) and (b)). (c) corresponds to a wire with the cross-section in the $x - y$ plane (an $x - z$ wire has identical dispersion) while (d) corresponds to a wire with the cross-section in the $y - z$ plane. The insets show the geometry of the wire in each case.

The setup studied here (see scheme in Fig. 5.4(g)) is typically used in Hall measurements and allow for the determination of the longitudinal and Hall resistances associated with the edge states. Furthermore, a planar architecture for the contacts may offer advantages, such as easier gating and tuning, over three-dimensional counterparts. Such contacts problems together with difficulty in tuning the Weyl semimetals themselves [15]. In our case, we would like to determine the fingerprints of the topology of this 3D system in the transport response measured at a surface. The answer is a priori not obvious since the states associated to the Fermi arcs are surface states, and not edge states as in a Chern insulator. Interestingly, one could also study the crossover between those two cases by varying the dimension of the cuboid so that it becomes 2D (we will come back to this when discussing Fig. 5.5), a transition that has elicited much interest [60, 80].

Our numerical simulations are restricted to the coherent regime, where scattering theory is valid. Specifically, we apply the Landaüer-Buttiker formalism [74] to this three-dimensional system (see schemes in Fig. 5.4(g)) with the aid of the Kwant module [77]. Fig. 5.4 shows the two-terminal (panel a), longitudinal (panel b) and Hall conductances (panel c) as a function of the Fermi energy in the zero-temperature limit. These results correspond to a setup where the leads are attached to the yz surface. We emphasize that our results (as well as those of Ref. [78]) correspond to conductances rather than conductivities as calculated by other authors [81, 82]. In the latter case, since they are bulk quantities, the effect of Fermi arcs are less evident.

In the first place, as shown in Fig. 5.4(c), we find a nearly-quantized Hall conductance $\sigma_{yz} \simeq \frac{e^2}{h}$. This value of the Hall conductance is connected with the Chern number $\nu = -1$ on the plane in the Brillouin zone that is outside the Weyl nodes because the planes with non-zero Chern number can be regarded as the stacking of 2D Chern insulators in a quantum Hall effect phase [16]. The differences between the simulated values and perfect quantization are in the order of 10^{-7}, this is $\sigma_{yz} - \frac{e^2}{h} \simeq \times 10^{-7}$, except at a few discrete points that coincide with the onset of new subbands either in the semimetal or in the leads.

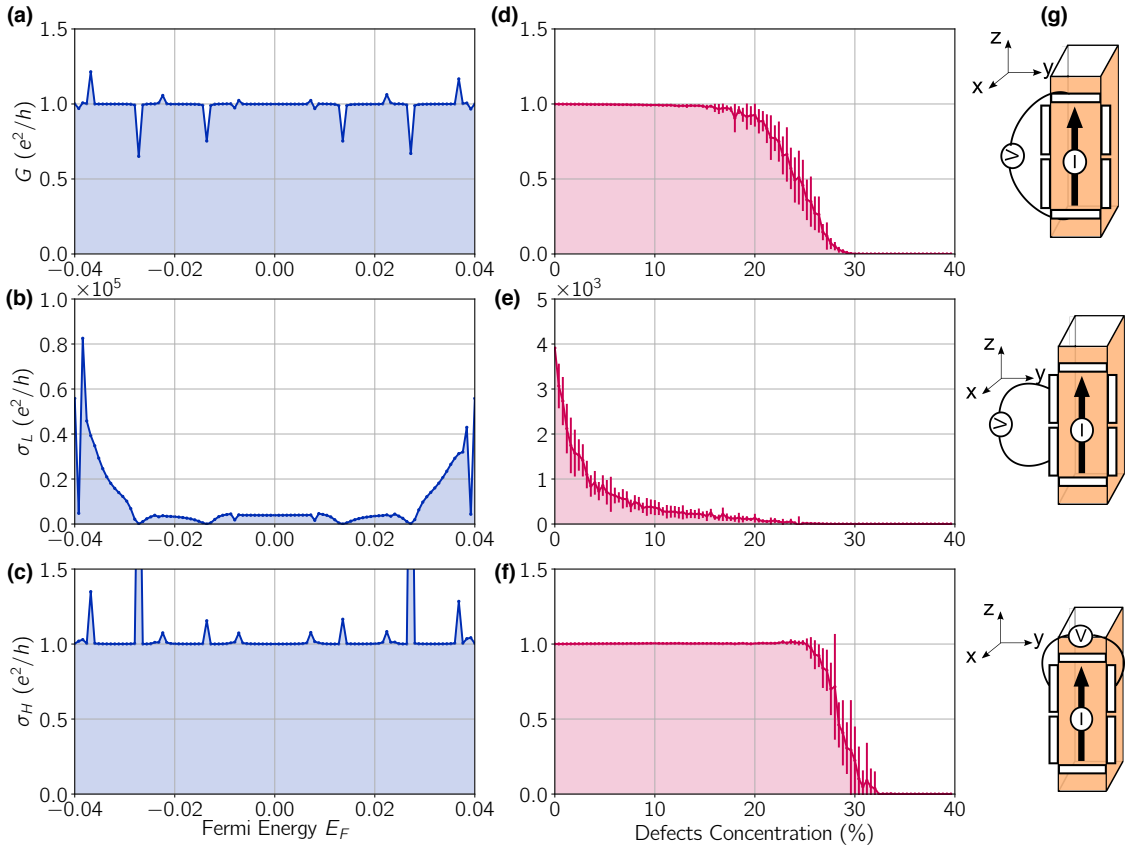

Figure 5.4: Transport response at the surface of the yz face of a rectangular cuboid. Six electrical contacts in an H configuration access the yz plane as shown in (g). (a) Two-terminal conductance G, (b) Longitudinal conductance σ_L, and (c) Hall conductance σ_H, are plotted against the Fermi Energy E_f set on the leads. Panels (d), (e) and (f) show the same magnitudes as their counterparts on the left but averaged over 15 indepedent realizations of disorder as a function of the concentration of defects (vacancies) and for $E_F = 0.001$. The bars depict the fluctuations around the average values. The setups are represented in the schemes in (g), note that the contacts are two-dimensional.

The non-vanishing value of the Hall conductance even in the absence of an external magnetic field is a consequence of the intrinsic breaking of time reversal symmetry in our model Hamiltonian, i.e. by the role played by the parameter m, much as in the (anomalous) quantum Hall effect [83, 84]. But besides this similarity, there are also differences that we point out below. They concern the longitudinal conductivity and the robustness to disorder.

In addition, we observe a non-vanishing longitudinal conductance as shown in Fig. 5.4(b). This is connected with the observed small deviations from perfect quantization of the Hall conductance and can be interpreted in terms of the finite and non-vanishing penetration length of the surface states, which decay exponentially into the bulk.

To get further insight, we test the robustness of these results to defects. To such end, we add vacancies at random within to the sample and computed how the two-terminal, longitudinal and Hall conductances changed in the same setup. The results are shown in the panels (d), (e) and (f) of Fig. 5.4, averaged 15 realizations of disorder. For a given defects concentration one chooses a set of sites and transform them into vacancies. The results turn out to be remarkably robust to disorder, with the conductance being substantially reduced only at about 25% of defects. This is much higher than expected, for example, in the two-dimensional Haldane model [23].

Indeed, an interesting question is how does the transport response evolve as the cuboid becomes thinner and, eventually, two-dimensional. In the present setup this can be done without changing the measurement

probes which are on the surface. Fig. 5.5 shows the results for the two-terminal conductance G, the longitudinal conductance σ_L, and the hall conductance σ_H (computed at $E_F = 0.001$) as a function of the dimension of the cuboid along x, N. N spans from the two-dimensional limit ($N = 1$) to $N = 30$ as used in Fig. 5.4.

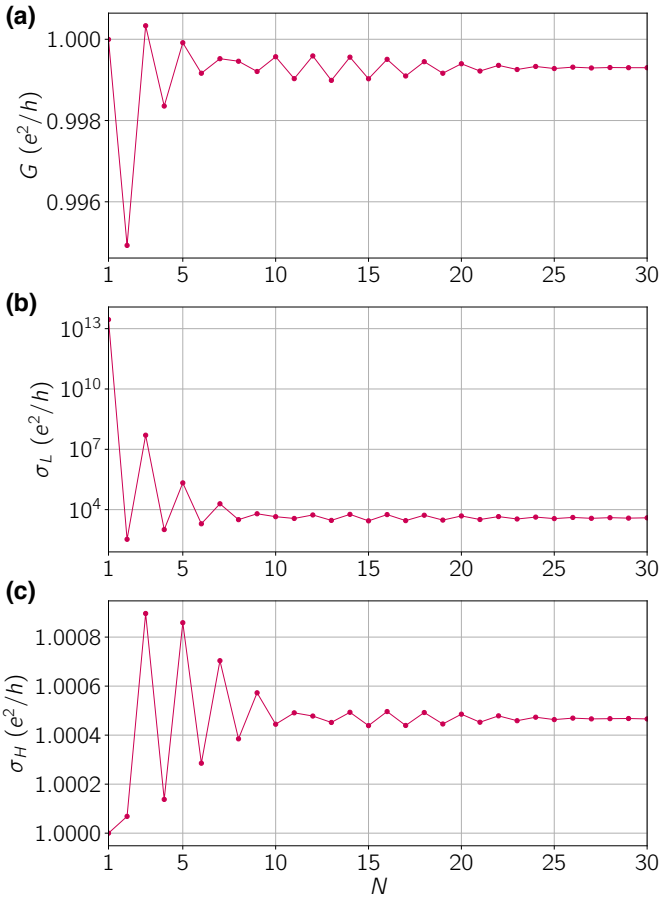

Figure 5.5: In this figure we explore how G (a), σ_L (b), and σ_H (c), determined from probes on the yz face as in the previous figure, change as the dimension of the Weyl semimetal along x, N, is varied. Here, we set $E_F = 0.001$.

Figure 5.5 shows that in the two-dimensional limit transport occurs as in a Chern insulator, with the Hall conductance being perfectly quantized and a vanishing longitudinal resistance. This picture changes as the sample becomes thicker until it converges to a situation where the Hall conductance aparts itself slightly from the perfect quantization with the concomitant non-vanishing longitudinal resistance. Besides clarifying the effect of the sample size on our previous results, this figure highlights the role of the dimensionality and the effect of the penetration of the surface states into the bulk.

To complete our analysis we study the transport response on the xy plane (the same results are obtained for the xz plane). We find that there is no Hall conductance response and that $\sigma_{xx} \ll \sigma_{yy}$ as shown in Fig. 5.6(a). These results are a consequence of the dispersion shown in Fig. 5.3(a) and (b). The Fermi arcs have group velocity in the y and z directions only, and thus do not allow for transport in the x direction. The previous results motivate us to analyze how do the currents flow in a finite sample of the semimetal. Since transport is impeded in the x direction, there also should not be current density flowing along x.

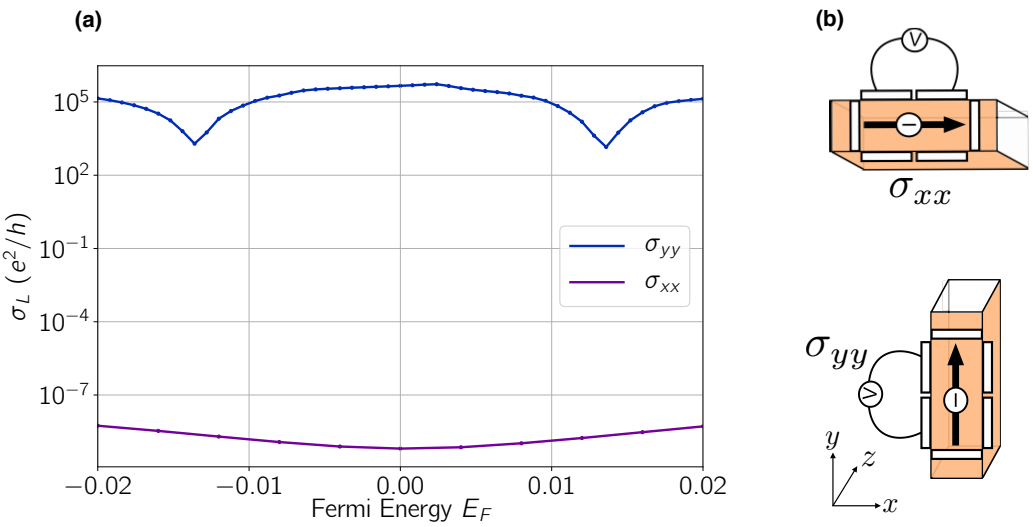

Figure 5.6: Transport response at the surface of the xy face of a rectangular cuboid. Six electrical contacts in an H configuration access the xy plane. (a) Longitudinal conductance σ_L is plotted against the Fermi Energy E_F set on the leads for two different orientations of the cuboid geometry, thus measuring either σ_{yy} or σ_{xx} as shown in panel (b).

5.4 Chiral States and Persistent Currents

Inspired by the previous conclusion, we calculate the bond currents [85] at $E_f = 0$ for a finite sample of the semimetal. We find that even in the absence of an external magnetic field, the system develops persistent currents around the x axis. These currents flow through the boundary of the semimetal as shown schematically in Fig. 5.7. We attribute these results to the time-reversal breaking acting as an intrinsic magnetic field pointing parallel to the Fermi arcs. The currents in the system are only of the solenoid type; transport along the x axis is impeded in the pristine system (the states at the boundary are dispersionless), thereby producing a very high longitudinal resistance in the x direction compared to the other directions. This picture helps to explain our transport results.

The above picture is still not quantative. Figure 5.8 (a) shows the magnitude of the maximum surface current (maximum bond current) as a function of the time reversal breaking parameter m. Different curves correspond to different system sizes of a $N \times N \times N$ cube. The horizontal axis ranged at $m = 0.5$, the value which signals the beginning of the topological phase. Figure 5.8 (b) shows a detail of the current dependence with the system size at fixed $m = 1.0$.

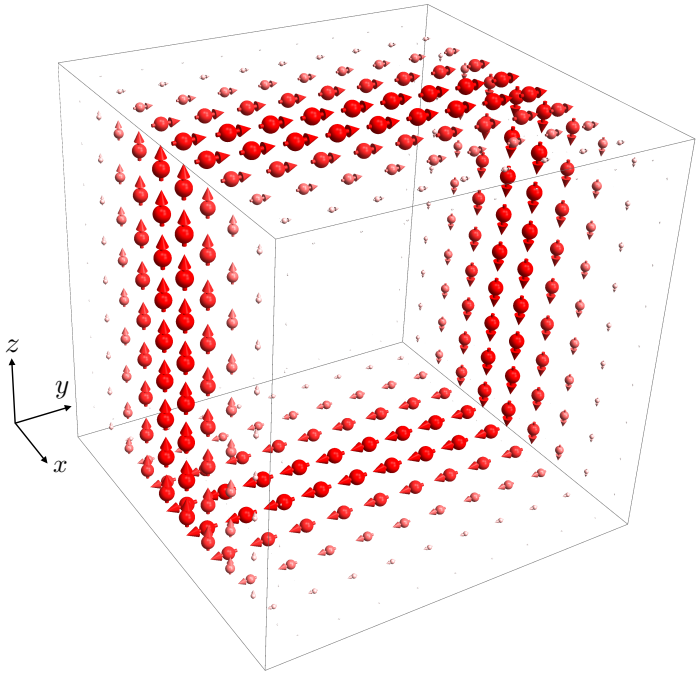

Figure 5.7: Scheme showing the current density flow in a finite sample of Weyl Semimetal $10 \times 10 \times 10$ lattice sites, at $E_F = 0$. The arrows point in the direction of the current flow, and their size and color intensity are proportional to the magnitude of the current density.

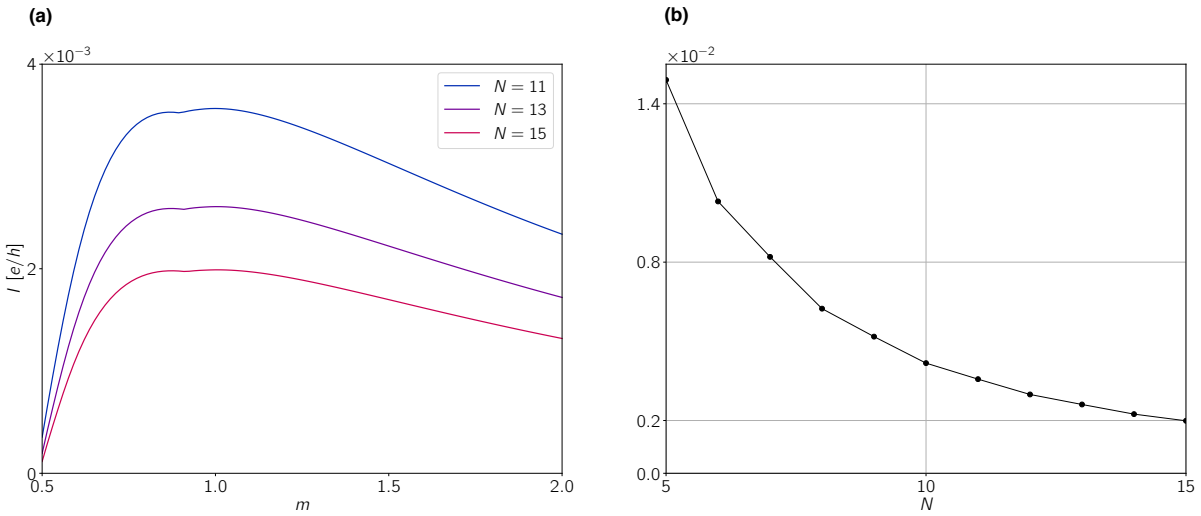

Figure 5.8: (a) Maximum surface current for a cube of $N \times N \times N$ lattice sites as a function of m, the time reversal breaking parameter. (b) Maximum surface current as a function of the cube lateral dimension N at fixed $m = 1.0$.

Chapter 6

Final Remarks

In summary, we have explored the multiterminal transport properties of a minimal model of a Weyl semimetal with broken time-reversal symmetry in the research carried in this thesis. This kind of hydrogen-atom model of a Weyl semimetal allows for simplified analysis. Our results show a nearly quantized Hall conductance, a result that holds up to remarkably high concentrations of disorder. Interestingly, in contrast with the quantum Hall effect studied in time-reversal invariant Weyl semimetals, the Hall response in our time-reversal broken model is not associated to the formation of edge states (at the surface of the Weyl semimetal) but rather to the surface states.

In addition, we have connected the dequantization of the Hall response with the unavoidable leak of these surface states into the bulk of the semimetal. Another significant result of this thesis is the retrieval of the quantization in the Hall conductance in the thin-film limit, which shows how the tridimensional geometry of semimetals sets foot for the appearance of the topological surface states. Also, we have demonstrated how persistent currents arise associated with these surface states in the absence of an external magnetic field, a signature of TRS breaking Weyl semimetals.

Being impervious to disorder, the transport properties of the surfaces of a Weyl semimetal have a great potential in applications in nanotechnological devices. In this way, the calculations in this thesis provide the motivation and are the starting point of new simulations required to elucidate the role of finite geometries upon the transport properties of more complex Weyl semimetals, in particular, of the TRS breaking type.

Recently this year, the discovery of a TRS breaking type of Weyl semimetal in the laboratory [13] has opened up the path to further understanding the peculiarities of the topological properties unique to these type of semimetals. We hope that in the next years, we see both an experimental confirmation of the calculations done on this thesis and the appearance of new unknown phenomena that will push the research on this topic.

Finally, we must mention that all the research done on this thesis was published last year in [75].

Bibliography

[1] Pavan Hosur and Xiaoliang Qi. "Recent developments in transport phenomena in Weyl semimetals". In: *Comptes Rendus Physique* 14.9 (2013). Topological insulators / Isolants topologiques, pp. 857 –870. ISSN: 1631-0705. DOI: https://doi.org/10.1016/j.crhy.2013.10.010.

[2] Oskar Vafek and Ashvin Vishwanath. "Dirac Fermions in Solids: From High-Tc Cuprates and Graphene to Topological Insulators and Weyl Semimetals". In: *Annual Review of Condensed Matter Physics* 5.1 (2014), pp. 83–112. DOI: 10.1146/annurev-conmatphys-031113-133841. eprint: https://doi.org/10.1146/annurev-conmatphys-031113-133841.

[3] Binghai Yan and Claudia Felser. "Topological Materials: Weyl Semimetals". In: *Annual Review of Condensed Matter Physics* 8.1 (2017), pp. 337–354. DOI: 10.1146/annurev-conmatphys-031016-025458. eprint: https://doi.org/10.1146/annurev-conmatphys-031016-025458.

[4] Shuang Jia, Su-Yang Xu, and M. Zahid Hasan. "Weyl semimetals, Fermi arcs and chiral anomalies". In: *Nature Materials* 15 (Oct. 2016), 1140 EP –.

[5] S. A. Parameswaran et al. "Probing the Chiral Anomaly with Nonlocal Transport in Three-Dimensional Topological Semimetals". In: *Phys. Rev. X* 4 (3 2014), p. 031035. DOI: 10.1103/PhysRevX.4.031035.

[6] Ching-Kit Chan et al. "When Chiral Photons Meet Chiral Fermions: Photoinduced Anomalous Hall Effects in Weyl Semimetals". In: *Phys. Rev. Lett.* 116 (2 2016), p. 026805. DOI: 10.1103/PhysRevLett.116.026805.

[7] Y. H. Wang et al. "Observation of Floquet-Bloch States on the Surface of a Topological Insulator". In: *Science* 342.6157 (2013), pp. 453–457. ISSN: 0036-8075. DOI: 10.1126/science.1239834. eprint: http://science.sciencemag.org/content/342/6157/453.full.pdf.

[8] Ching-Kit Chan et al. "Photocurrents in Weyl semimetals". In: *Phys. Rev. B* 95 (4 2017), p. 041104. DOI: 10.1103/PhysRevB.95.041104.

[9] Su-Yang Xu et al. "Discovery of a Weyl fermion semimetal and topological Fermi arcs". In: *Science* 349.6248 (2015), pp. 613–617. ISSN: 0036-8075. DOI: 10.1126/science.aaa9297. eprint: http://science.sciencemag.org/content/349/6248/613.full.pdf.

[10] Ling Lu et al. "Experimental observation of Weyl points". In: *Science* 349.6248 (2015), pp. 622–624. ISSN: 0036-8075. DOI: 10.1126/science.aaa9273. eprint: http://science.sciencemag.org/content/349/6248/622.full.pdf.

[11] B. Q. Lv et al. "Experimental Discovery of Weyl Semimetal TaAs". In: *Phys. Rev. X* 5 (3 2015), p. 031013. DOI: 10.1103/PhysRevX.5.031013.

[12] Barry Bradlyn et al. "Beyond Dirac and Weyl fermions: Unconventional quasiparticles in conventional crystals". In: *Science* 353.6299 (2016). ISSN: 0036-8075. DOI: 10.1126/science.aaf5037. eprint: http://science.sciencemag.org/content/353/6299/aaf5037.full.pdf.

[13] Sergey Borisenko et al. "Time-reversal symmetry breaking type-II Weyl state in YbMnBi2". In: *Nature Communications* 10.1 (2019), p. 3424.

[14] R D dos Reis et al. "On the search for the chiral anomaly in Weyl semimetals: the negative longitudinal magnetoresistance". In: *New Journal of Physics* 18.8 (2016), p. 085006.

[15] Ilya Belopolski et al. "Discovery of a new type of topological Weyl fermion semimetal state in MoxW1?xTe2". In: *Nature Communications* 7 (Dec. 2016), 13643 EP –.

[16] Kai-Yu Yang, Yuan-Ming Lu, and Ying Ran. "Quantum Hall effects in a Weyl semimetal: Possible application in pyrochlore iridates". In: *Phys. Rev. B* 84 (7 2011), p. 075129. DOI: 10.1103/PhysRevB.84.075129.

[17] P Baireuther et al. "Scattering theory of the chiral magnetic effect in a Weyl semimetal: interplay of bulk Weyl cones and surface Fermi arcs". In: *New Journal of Physics* 18.4 (2016), p. 045009.

[18] Akira Igarashi and Mikito Koshino. "Magnetotransport in Weyl semimetal nanowires". In: *Phys. Rev. B* 95 (19 2017), p. 195306. DOI: 10.1103/PhysRevB.95.195306.

[19] C. M. Wang et al. "3D Quantum Hall Effect of Fermi Arcs in Topological Semimetals". In: *Phys. Rev. Lett.* 119 (13 2017), p. 136806. DOI: 10.1103/PhysRevLett.119.136806.

[20] Pavan Hosur, S. A. Parameswaran, and Ashvin Vishwanath. "Charge Transport in Weyl Semimetals". In: *Phys. Rev. Lett.* 108 (4 2012), p. 046602. DOI: 10.1103/PhysRevLett.108.046602.

[21] S. Nandy et al. "Chiral Anomaly as the Origin of the Planar Hall Effect in Weyl Semimetals". In: *Phys. Rev. Lett.* 119 (17 2017), p. 176804. DOI: 10.1103/PhysRevLett.119.176804.

[22] E. V. Gorbar et al. "Origin of dissipative Fermi arc transport in Weyl semimetals". In: *Phys. Rev. B* 93 (23 2016), p. 235127. DOI: 10.1103/PhysRevB.93.235127.

[23] Eduardo V. Castro, M. Pilar López-Sancho, and María A. H. Vozmediano. "Anderson localization and topological transition in Chern insulators". In: *Phys. Rev. B* 92 (8 2015), p. 085410. DOI: 10.1103/PhysRevB.92.085410.

[24] B. Bernevig. *Topological Insulators and Topological Superconductors*. Princeton University Press, 2013.

[25] Molenkamp L. Franz M. *Contemporary Concepts of Condensed Matter Science: Topological Insulators. Volume 6*. Elsevier, 2013.

[26] Oroszlány L. Asbóth J. and Pályi A. *A Short Course on Topological Insulators. Band Structure and Edge States in One and Two Dimensions*. Springer International Publisher, 2016.

[27] M. Z. Hasan and C. L. Kane. "Colloquium: Topological insulators". In: *Rev. Mod. Phys.* 82 (4 2010), pp. 3045–3067. DOI: 10.1103/RevModPhys.82.3045.

[28] M. Zahid Hasan and Joel E. Moore. "Three-Dimensional Topological Insulators". In: *Annual Review of Condensed Matter Physics* 2.1 (2011), pp. 55–78. DOI: 10.1146/annurev-conmatphys-062910-140432. eprint: https://doi.org/10.1146/annurev-conmatphys-062910-140432.

[29] Nakahara M. *Geometry, Topology and Physics*. Institute of Physics Publishing, 2003.

[30] M. V. Berry. "Quantal phase factors accompanying adiabatic changes". In: *A. Mathematical and Physical Sciences* 392 (1984).

[31] K. v. Klitzing, G. Dorda, and M. Pepper. "New Method for High-Accuracy Determination of the Fine-Structure Constant Based on Quantized Hall Resistance". In: *Phys. Rev. Lett.* 45 (6 1980), pp. 494–497. DOI: 10.1103/PhysRevLett.45.494.

[32] Klaus von Klitzing. "The quantized Hall effect". In: *Rev. Mod. Phys.* 58 (3 1986), pp. 519–531. DOI: 10.1103/RevModPhys.58.519.

[33] D. J. Thouless et al. "Quantized Hall Conductance in a Two-Dimensional Periodic Potential". In: *Phys. Rev. Lett.* 49 (6 1982), pp. 405–408. DOI: 10.1103/PhysRevLett.49.405.

[34] Xiao-Liang Qi, Yong-Shi Wu, and Shou-Cheng Zhang. "Topological quantization of the spin Hall effect in two-dimensional paramagnetic semiconductors". In: *Phys. Rev. B* 74 (8 2006), p. 085308. DOI: 10.1103/PhysRevB.74.085308.

[35] H. Bruus and K. Flensberg. *Many-body Quantum Theory in Condensed Matter Physics*. Oxford University Press, 2004.

[36] Akkermans E. and G. Montambaux. *Mesoscopic Physics of Electrons and Photons*. Cambridge University Press, 2007.

[37] Cayssol J. "Introduction to Dirac materials and topological insulators". In: *Comptes Rendus Physique* 14.9 (2013). Topological insulators / Isolants topologiques, pp. 760 –778. ISSN: 1631-0705. DOI: https://doi.org/10.1016/j.crhy.2013.09.012.

[38] C. L. Kane and E. J. Mele. "Quantum Spin Hall Effect in Graphene". In: *Phys. Rev. Lett.* 95 (22 2005), p. 226801. DOI: 10.1103/PhysRevLett.95.226801.

[39] C. L. Kane and E. J. Mele. "Z_2 Topological Order and the Quantum Spin Hall Effect". In: *Phys. Rev. Lett.* 95 (14 2005), p. 146802. DOI: 10.1103/PhysRevLett.95.146802.

[40] B. Andrei Bernevig, Taylor L. Hughes, and Shou-Cheng Zhang. "Quantum Spin Hall Effect and Topological Phase Transition in HgTe Quantum Wells". In: *Science* 314.5806 (2006), pp. 1757–1761. ISSN: 0036-8075. DOI: 10.1126/science.1133734. eprint: https://science.sciencemag.org/content/314/5806/1757.full.pdf.

[41] Markus König et al. "Quantum Spin Hall Insulator State in HgTe Quantum Wells". In: *Science* 318.5851 (2007), pp. 766–770. ISSN: 0036-8075. DOI: 10.1126/science.1148047. eprint: https://science.sciencemag.org/content/318/5851/766.full.pdf.

[42] J. E. Moore and L. Balents. "Topological invariants of time-reversal-invariant band structures". In: *Phys. Rev. B* 75 (12 2007), p. 121306. DOI: 10.1103/PhysRevB.75.121306.

[43] Rahul Roy. "Topological phases and the quantum spin Hall effect in three dimensions". In: *Phys. Rev. B* 79 (19 2009), p. 195322. DOI: 10.1103/PhysRevB.79.195322.

[44] Liang Fu, C. L. Kane, and E. J. Mele. "Topological Insulators in Three Dimensions". In: *Phys. Rev. Lett.* 98 (10 2007), p. 106803. DOI: 10.1103/PhysRevLett.98.106803.

[45] Liang Fu and C. L. Kane. "Topological insulators with inversion symmetry". In: *Phys. Rev. B* 76 (4 2007), p. 045302. DOI: 10.1103/PhysRevB.76.045302.

[46] D. Hsieh et al. "A topological Dirac insulator in a quantum spin Hall phase". In: *Nature* 452 (Apr. 2008), 970 EP –.

[47] Y. Xia et al. "Observation of a large-gap topological-insulator class with a single Dirac cone on the surface". In: *Nature Physics* 5 (May 2009), 398 EP –.

[48] Haijun Zhang et al. "Topological insulators in Bi2Se3, Bi2Te3 and Sb2Te3 with a single Dirac cone on the surface". In: *Nature Physics* 5 (May 2009), 438 EP –.

[49] K. S. Novoselov et al. "Two-dimensional gas of massless Dirac fermions in graphene". In: *Nature* 438.7065 (2005), pp. 197–200. DOI: 10.1038/nature04233.

[50] Charlier J-C. Foa Torres L. E. F. Roche S. *Introduction to Graphene-Based Nanomaterials. From Electronic Structure to Quantum Transport.* Cambridge University Press, 2014.

[51] Tsuneya Ando, Takeshi Nakanishi, and Riichiro Saito. "Berry's Phase and Absence of Back Scattering in Carbon Nanotubes". In: *Journal of the Physical Society of Japan* 67.8 (1998), pp. 2857–2862. DOI: 10.1143/JPSJ.67.2857. eprint: https://doi.org/10.1143/JPSJ.67.2857.

[52] H.B. Nielsen and M. Ninomiya. "Absence of neutrinos on a lattice: (I). Proof by homotopy theory". In: *Nuclear Physics B* 185.1 (1981), pp. 20 –40. ISSN: 0550-3213. DOI: https://doi.org/10.1016/0550-3213(81)90361-8.

[53] Itzykson C. and Drouffe J-M. *Statistical field theory. Volume 1. From Brownian Motion to Renormalization and Lattice Gauge Theory.* Cambridge University Press, 1989.

[54] Shuichi Murakami. "Phase transition between the quantum spin Hall and insulator phases in 3D: emergence of a topological gapless phase". In: *New Journal of Physics* 9.9 (2007), pp. 356–356. DOI: 10.1088/1367-2630/9/9/356.

[55] Xiangang Wan et al. "Topological semimetal and Fermi-arc surface states in the electronic structure of pyrochlore iridates". In: *Phys. Rev. B* 83 (20 2011), p. 205101. DOI: 10.1103/PhysRevB.83.205101.

[56] Pavan Hosur. "Friedel oscillations due to Fermi arcs in Weyl semimetals". In: *Phys. Rev. B* 86 (19 2012), p. 195102. DOI: 10.1103/PhysRevB.86.195102.

[57] J. W. McClure. "Diamagnetism of Graphite". In: *Phys. Rev.* 104 (3 1956), pp. 666–671. DOI: 10.1103/PhysRev.104.666.

[58] H.B. Nielsen and Masao Ninomiya. "The Adler-Bell-Jackiw anomaly and Weyl fermions in a crystal". In: *Physics Letters B* 130.6 (1983), pp. 389 –396. ISSN: 0370-2693. DOI: https://doi.org/10.1016/0370-2693(83)91529-0.

[59] Gang Xu et al. "Chern Semimetal and the Quantized Anomalous Hall Effect in $HgCr_2Se_4$". In: *Phys. Rev. Lett.* 107 (18 2011), p. 186806. DOI: 10.1103/PhysRevLett.107.186806.

[60] A. A. Burkov and Leon Balents. "Weyl Semimetal in a Topological Insulator Multilayer". In: *Phys. Rev. Lett.* 107 (12 2011), p. 127205. DOI: 10.1103/PhysRevLett.107.127205.

[61] Adolfo G. Grushin. "Consequences of a condensed matter realization of Lorentz-violating QED in Weyl semi-metals". In: *Phys. Rev. D* 86 (4 2012), p. 045001. DOI: 10.1103/PhysRevD.86.045001.

[62] Yan Sun et al. "Strong Intrinsic Spin Hall Effect in the TaAs Family of Weyl Semimetals". In: *Phys. Rev. Lett.* 117 (14 2016), p. 146403. DOI: 10.1103/PhysRevLett.117.146403.

[63] Stephen L. Adler. "Axial-Vector Vertex in Spinor Electrodynamics". In: *Phys. Rev.* 177 (5 1969), pp. 2426–2438. DOI: 10.1103/PhysRev.177.2426.

[64] J. S. Bell and R. Jackiw. "A PCAC puzzle: $\pi^0 \to \gamma\gamma$ in the σ-model". In: *Il Nuovo Cimento A (1965-1970)* 60.1 (1969), pp. 47–61. ISSN: 1826-9869. DOI: 10.1007/BF02823296.

[65] D. T. Son and B. Z. Spivak. "Chiral anomaly and classical negative magnetoresistance of Weyl metals". In: *Phys. Rev. B* 88 (10 2013), p. 104412. DOI: 10.1103/PhysRevB.88.104412.

[66] Tay-Rong Chang et al. "Prediction of an arc-tunable Weyl Fermion metallic state in MoxW1?xTe2". In: *Nature Communications* 7 (Feb. 2016), 10639 EP –.

[67] Yuval Baum et al. "Current at a Distance and Resonant Transparency in Weyl Semimetals". In: *Phys. Rev. X* 5 (4 2015), p. 041046. DOI: 10.1103/PhysRevX.5.041046.

[68] B. Q. Lv et al. "Observation of Weyl nodes in TaAs". In: *Nature Physics* 11 (Aug. 2015), 724 EP –.

[69] L. X. Yang et al. "Weyl semimetal phase in the non-centrosymmetric compound TaAs". In: *Nature Physics* 11 (Aug. 2015), 728 EP –.

[70] Su-Yang Xu et al. "Discovery of a Weyl fermion state with Fermi arcs in niobium arsenide". In: *Nature Physics* 11 (Aug. 2015), 748 EP –.

[71] Su-Yang Xu et al. "Experimental discovery of a topological Weyl semimetal state in TaP". In: *Science Advances* 1.10 (2015). DOI: 10.1126/sciadv.1501092. eprint: https://advances.sciencemag.org/content/1/10/e1501092.full.pdf.

[72] Yigal Meir and Ned S. Wingreen. "Landauer formula for the current through an interacting electron region". In: *Phys. Rev. Lett.* 68 (16 1992), pp. 2512–2515. DOI: 10.1103/PhysRevLett.68.2512.

[73] Mahan G. *Many-Particle Physics*. Cambridge University Press, 2000.

[74] Datta S. *Electronic Transport in Mesoscopic Systems*. Cambridge University Press, 1997.

[75] J. Chesta Lopez, L. E. F. Foa Torres, and A. S. Nunez. "Multiterminal conductance at the surface of a Weyl semimetal". In: *Phys. Rev. B* 97 (12 2018), p. 125419. DOI: 10.1103/PhysRevB.97.125419.

[76] Fritz Haake. "Time Reversal and Unitary Symmetries". In: *Quantum Signatures of Chaos*. Berlin, Heidelberg: Springer Berlin Heidelberg, 2001, pp. 15–36. ISBN: 978-3-662-04506-0. DOI: 10.1007/978-3-662-04506-0_2.

[77] Christoph W Groth et al. "Kwant: a software package for quantum transport". In: *New Journal of Physics* 16.6 (2014), p. 063065. DOI: 10.1088/1367-2630/16/6/063065.

[78] Yositake Takane. "Disorder Effect on Chiral Edge Modes and Anomalous Hall Conductance in Weyl Semimetals". In: *Journal of the Physical Society of Japan* 85.12 (2016), p. 124711. DOI: 10.7566/JPSJ.85.124711. eprint: https://doi.org/10.7566/JPSJ.85.124711.

[79] Koji Kobayashi et al. "Dimensional crossover of transport characteristics in topological insulator nanofilms". In: *Phys. Rev. B* 92 (23 2015), p. 235407. DOI: 10.1103/PhysRevB.92.235407.

[80] Kazuki Yokomizo and Shuichi Murakami. "Topological phases in a Weyl semimetal multilayer". In: *Phys. Rev. B* 95 (15 2017), p. 155101. DOI: 10.1103/PhysRevB.95.155101.

[81] Chui-Zhen Chen et al. "Disorder and Metal-Insulator Transitions in Weyl Semimetals". In: *Phys. Rev. Lett.* 115 (24 2015), p. 246603. DOI: 10.1103/PhysRevLett.115.246603.

[82] Hassan Shapourian and Taylor L. Hughes. "Phase diagrams of disordered Weyl semimetals". In: *Phys. Rev. B* 93 (7 2016), p. 075108. DOI: 10.1103/PhysRevB.93.075108.

[83] F. D. M. Haldane. "Model for a Quantum Hall Effect without Landau Levels: Condensed-Matter Realization of the "Parity Anomaly"". In: *Phys. Rev. Lett.* 61 (18 1988), pp. 2015–2018. DOI: 10.1103/PhysRevLett.61.2015.

[84] Naoto Nagaosa et al. "Anomalous Hall effect". In: *Rev. Mod. Phys.* 82 (2 2010), pp. 1539–1592. DOI: 10.1103/RevModPhys.82.1539.

[85] Tchavdar N Todorov. "Tight-binding simulation of current-carrying nanostructures". In: *Journal of Physics: Condensed Matter* 14.11 (2002), pp. 3049–3084. DOI: 10.1088/0953-8984/14/11/314.